ROYAL SOCIETY
OF CHEMISTRY

PAPER

Check for updates

A poly(3,4-propylenedioxythiophene)/carbon micro-sphere-bismuth nanoflake composite and multifunctional Co-doped graphene for a benchmark photo-supercapacitor†

Aparajita Das, Manoranjan Ojha, Palyam Subramanyam and Melepurath Deepa [iD] *

Efficient storage of sunlight in the form of charge is accomplished by designing and implementing a photo-supercapacitor (PSC) with a novel, cost-effective architecture. Sulfur (S)- and nitrogen (N)-doped graphene particles (SNGPs) are incorporated in a TiO_2/CdS photoanode. The beneficial effects of SNGPs such as the high electrical conductance promoting fast electron transfer to TiO_2, a suitably positioned conduction band that maximizes charge separation, and its' ability to absorb red photons translate into a power conversion efficiency of 9.4%, for the champion cell. A new composite of poly(3,4-propylenedioxythiophene)/carbon micro-sphere-bismuth nanoflakes (PProDOT/CMS-BiNF) is integrated with the photoanode to yield the PSC. The photocurrent produced under 1 sun irradiance is directed to the supercapacitor, wherein, the synergy between the faradaic and electrical double layer charge accumulation mechanisms of PProDOT and CMS-BiNF bestows storage parameters of an areal capacitance of 104.6 mF cm^{-2}, and energy and power densities of 9 μW h cm^{-2} and 0.026 mW cm^{-2}. An overall photo-conversion and storage efficiency of 6.8% and an energy storage efficiency of 72% exhibited by the PSC are much superior to those delivered by a majority of the PSCs reported in the literature on the otherwise highly efficient perovskite solar cell or the expensive Ru dye based solar cells.

1. Introduction

To meet the ever-increasing global energy requirements, the prospect of fabricating low cost, easy to assemble single platform based dual function devices is in line with the current thrust on developing sustainable technologies for a better future. Aligned with this concept is the photo-supercapacitor (PSC), a device that combines the functions of light harvesting and storage in a single physical entity.[1,2] A PSC therefore is composed of a solar cell that converts solar radiation to current, which when channelized to a supercapacitor gets stored in the form of charge. Instead of having two separate devices for the two distinct functions, they can be efficiently assembled on a common current collector platform to yield the PSC. The challenge therefore is to be able to preserve a high power conversion efficiency (PCE) and high energy storage parameters while simultaneously maintaining a high overall photo-conversion and storage efficiency. This is a daunting task, for it

requires chemically compatible components to be chosen judiciously that can be assembled into an efficient cell architecture capable of delivering the aforesaid performance metrics. In a majority of reports on PSCs,[3–6] the photovoltaic (PV) part is primarily based on a Ru dye or the methylammonium lead iodide perovskite, owing to the high PCEs they can deliver,[7–12] and the storage electrodes are based on carbon nanotubes, conducting polymers like polypyrrole (PPy), polyaniline (PANI), and poly(3,4-ethylenedioxythiophene) (PEDOT) as well as titania nanostructures for they can yield high specific capacitances (SCs). Carbons store energy well due to a high number of electrochemically accessible active sites, attributed to their high effective surface areas and porous microstructures, and the conducting polymers/inorganic materials offer good redox activities and chemical stability towards long term cycling.[13]

Digressing from these popular choices for the PV and storage components, in this report, an inorganic semiconducting chalcogenide and doped graphene particles are used as co-sensitizers in the solar cell part. Graphene quantum dots (GQDs) as green photosensitizers in photovoltaic,[14] photocatalysis[15] and supercapacitor[16] applications are an exciting class of materials, for they are non-toxic, environment friendly, are capable of absorbing a broad spectral range, are chemically stable, offer high carrier mobility and tunable band gaps. Furthermore, by replacing some of the carbon atoms with

Department of Chemistry, Indian Institute of Technology Hyderabad, Kandi, 502285, Sangareddy, Telangana, India. E-mail: mdeepa@chy.iith.ac.in

† Electronic supplementary information (ESI) available: Figures for cyclic voltammograms of photoactive films, *J–V* plot of FTO/SNGP/CdS, Bode phase, LSV, CV and GCD plots of Bi nanoflakes, stability test of the solar cell. Tables of CB, VB data, five cell average, EIS data of photoanode and counter electrodes, literature survey for the overall efficiency of the PSC. See DOI: 10.1039/d0na00103a

hetero atoms like S and N in the graphitic lattice, more defect states are introduced, which modifies the electronic structure of graphene, and thus alters its' electrical, optical and physico-chemical properties.[17,18] Relying on this approach, in this study, sulfur (S) and nitrogen (N) doped graphene particles, labeled as SNGPs, were synthesized by a hydrothermal route, and anchored to the TiO_2 support, followed by CdS deposition to yield the high performing TiO_2/SNGP/CdS photoanode. A literature survey also confirms the ability of GQDs to serve as efficient photoactive materials.[19,20]

Besides the photoanode, the counter electrode (CE) of the solar cell also controls the PV response. An ideal CE should be electrically conducting and have a high surface area to bring about the electrocatalytic reduction of the oxidized species in the polysulfide/silica gel electrolyte. Conducting polymers (CPs), carbon nanomaterials, metal nanoparticles and their composites have been explored as CEs in solar cells,[21,22] and also as electroactive electrodes in supercapacitors.[23,24] Of the lesser studied conducting polymers is poly(3,4-propylenedioxythiophene) or PProDOT.[25] Lee et al.[25] used PProDOT-Et$_2$, PProDOT, PEDOT, and sputtered-Pt electrodes as CEs in dye sensitized solar cells (DSSCs) which showed PCEs of 7.88, 7.08, 3.93 and 7.77% respectively. PProDOT based cells were characterized by PCEs comparable to that achieved with a Pt CE, whereas with PEDOT, a lower PCE was obtained. Ahmad et al.[26] prepared nanoporous layers of PProDOT with three different ionic liquids and used them as CEs, and the PProDOT with the most hydrophobic ionic liquid dopant displayed good catalytic properties to result in a PCE > 9%, which was significantly higher than the other Pt free CEs. A composite CE of PEDOT/multiwalled CNTs in a Ru dye based DSSC showed a PCE, greater by 13% than the DSSC with a PEDOT CE. The higher PCE was ascribed to low charge transfer resistance at the PEDOT/MWCNT/electrolyte interface and high electrocatalytic activity for the reversible I_3^-/I^- redox reaction.[27] Rafique et al.[28] reported an Ag-PPy-functionalized MWCNT nanocomposite CE based DSSC, which delivered a PCE of 7.6%, higher than that obtained with a traditional Pt CE.

Other aspects of PProDOT such as fast redox switching and a lower oxidation potential than PEDOT etc. also validate its use in a supercapacitor.[29] However, during repeated charge–discharge cycling, the polymers suffer from swelling and shrinkage due to counter ion doping and de-doping, which imparts mechanical stress and can accelerate its' delamination from the current collector. Use of composites with carbons, can help in improving cycling life, for the carbon nanomaterial can buffer the volume change experienced by the polymer, also increase the mechanical strength of the electrode.[30] To this end, in a previous study, a PEDOT/graphene oxide (GO) composite based supercapacitor[31] showed a SC of ~115 F g^{-1} and an energy density of 13.6 W h kg^{-1} at a current density 0.3 A g^{-1}, significantly improved relative to the pristine polymer's storage properties, and assigned to the high surface area of GO that amplifies the faradaic reaction of the polymer. PProDOT/single-walled CNT (SWNTs), helically wrapped with conjugate poly[2,6-{1,5-bis(3-propoxysulfonicacidsodiumsalt)}naphthylene]ethynylene exhibited a 90% SC retention after 21 000 cycles, compared

to PProDOT, which retained only 84% of its' initial SC.[32] Nanocomposites of Ag/MnO_2/RGO showed a much higher SC of 467.5 F g^{-1} compared to MnO_2/RGO electrode (293.2 F g^{-1}). In this ternary nanocomposite, Ag nanoparticles improved the electrical conductivity and promoted electron transfer.[33]

Based on this background, a configuration with TiO_2/SNGP/CdS as the photoanode, and a new composite of PProDOT with carbon micro-spheres (CMS), and bismuth (Bi) nanoflakes (BiNF) as the CE as well as the energy storage electrode is proposed for a PSC. Through elaborate structural details coupled with optical, electrochemical and photo-electrochemical studies, the rationale for developing this PSC with a unique configuration and the potential it has for practical applications is illustrated.

2. Experimental

Chemicals used in all experiments, synthesis of S,N-doped graphene particles (SNGPs), fabrication of photoactive electrodes and instrumentation techniques are provided in detail in the ESI.† The complete fabrication process for the PProDOT/CMS-BiNF CE is shown in Scheme 1. Step-wise illustration for the fabrication of the PSC device is shown through photographs in Scheme 2.

2.1 Construction of the photo-supercapacitor (PSC)

The dimensions of the PSC comprising of a solar cell and the symmetric supercapacitor are 6 cm × 1.2 cm. It is made up of three physical electrodes: (1) a photoanode (TiO_2/SNGP/CdS) supported on FTO/glass, (2) two PProDOT or PProDOT/CMS or PProDOT/CMS-BiNF films of 1.25 cm × 1.2 cm dimensions coated on a common Ni foam current collector, separated by an uncoated area of 3.5 cm × 1.2 cm, where one serves as the CE for the solar cell, and the other is one of the supercapacitor electrodes and (3) the second electrode (PProDOT or PProDOT/CMS or PProDOT/CMS-BiNF) for the supercapacitor. The central portion of the common Ni foam remains uncoated to prevent the direct mixing of two different electrolytes. Thus, two sandwich structures are created on a long Ni foam substrate: (i) a TiO_2/SNGP/CdS–S/S^{2-}/silica gel-PProDOT/CMS-BiNF solar cell and (ii) a CMS-BiNF/PProDOT/$Li^+ClO_4^-$ gel/PProDOT/CMS-BiNF symmetric supercapacitor.

A polysulfide gel electrolyte is used in the solar cell and it was prepared by dispersing 5 wt% of silica powder in an aqueous solution of 1 M Na_2S and 1 M S, with continuous stirring in a beaker at room temperature. The yellow colored homogeneous, slightly turbid gel was poured into a cavity created by a parafilm spacer over the CE: PProDOT/CMS-BiNF film over the long Ni foam substrate. The TiO_2/SNGP/CdS electrode was placed with the film side facing inwards over the gel, to yield the solar cell part. For the supercapacitor part, a lithium ion conducting gel polymeric electrolyte was synthesized by dissolving PMMA (0.7 g) in the clear 1 M $LiClO_4$/PC (1 g in 10 mL) solution. After vigorous stirring at 80 °C for 8 h, a colorless transparent gel was obtained and it was cooled to ambient temperature. This gel was applied over a GF/D spacer, which was sandwiched
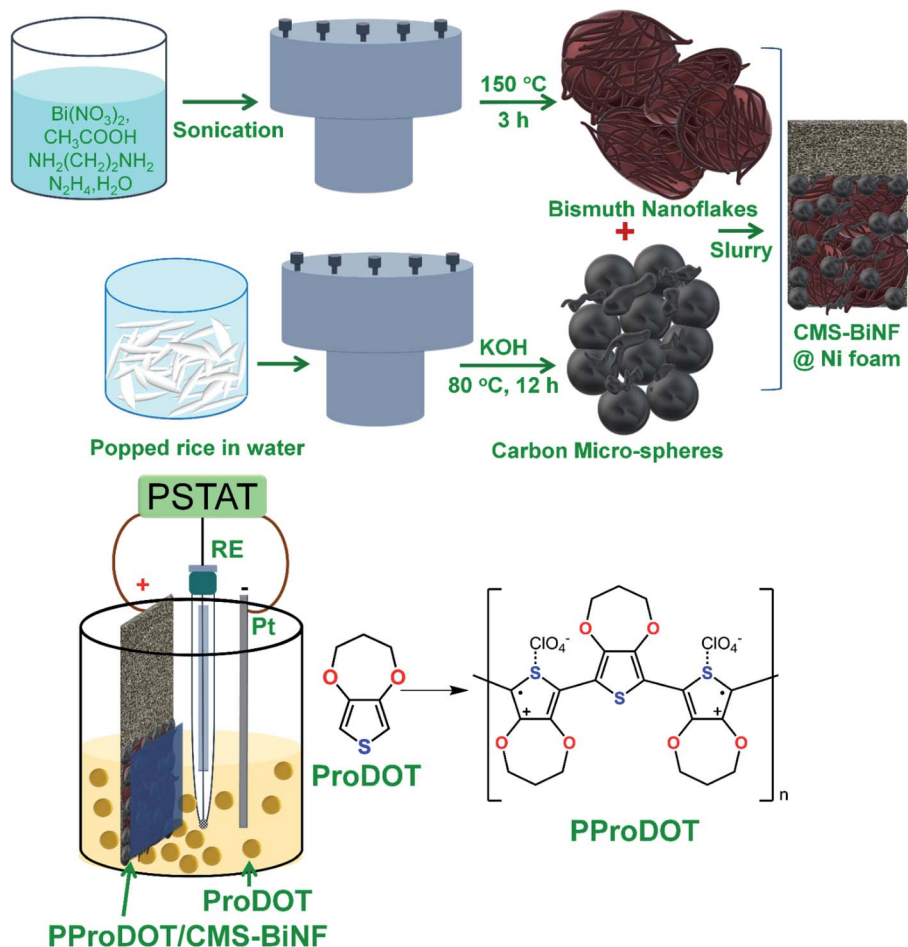
Scheme 1 Cartoon showing the preparation of the counter electrode for the QDSC.

between the two electrodes of the supercapacitor part of the PSC, placed over the PProDOT/CMS-BiNF@Ni foam end. Another PProDOT/CMS-BiNF electrode fabricated separately was affixed over the supercapacitor part of the cell (Scheme 2).

The labels (A), (B) and (C) in Scheme 2 are the three points for taking electrical connections for operating the PSC. The PSC cell was exposed from the rear side for all experiments involving irradiance. For all electrochemical and photoelectrochemical
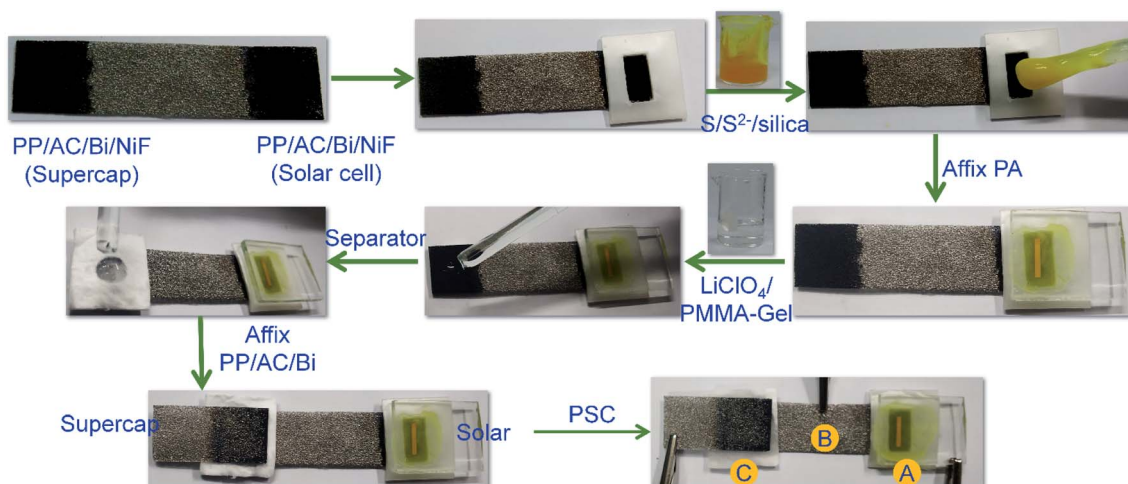
Scheme 2 Photographs showing PSC fabrication of the PSC.

measurements, a minimum of five electrodes of a given composition were tested.

The electrolytes used for both parts: the photovoltaic part, and the symmetric supercapacitor part are gels, which are highly viscous, and did not exhibit any visible sign of leakage, over long term operation. Leakage usually occurs if the gel is used in excess, the amount is optimized to prevent the oozing out of the gel. The gel used for the symmetric supercapacitor part has PMMA as the gelatinizing agent. PC is a non-volatile solvent with a high boiling point of 240 °C, and therefore this gel does not evaporate during operation. Further the gel is not only applied over the electrodes, but is also applied over a GF/D spacer which is 1.2 mm thick and has pores of ∼2.7 μm dimensions, and therefore, once the gel penetrates through the cross-section of the separator, its' proportion is ample for long term use. For the solar cell part, a polysulfide/silica gel electrolyte was used, where fumed silica assists in the formation of a quasi-solid state electrolyte and also restricts the photo-corrosion of the QDs. The spacer has a thickness of 2 mm, which allows a sufficient amount of gel to be incorporated between the two electrodes. Since this gel is not exposed, there is no distinct evaporation.

3. Results and discussion

3.1 Structural features of the PProDOT/CMS-BiNF composite

The ternary composite of PProDOT/CMS-BiNF coated on the Ni foam substrate is the key component of the PSC; for its serves as a CE for the photovoltaic part, and as the energy storage electrode for the supercapacitor. While the conducting polymer stores and releases energy by a faradaic mechanism, carbon micro-spheres and Bi nanoflakes do so *via* EDL formation, thus improving the overall activity of the composite. A SEM image of the PProDOT/CMS-BiNF composite is shown in Fig. 1a. Uncoated Ni foam shows a three dimensional cross linked porous structure with smooth flat fibers of Ni metal available for the electroactive PProDOT, carbon micro-spheres and Bi nanoflakes to anchor onto (inset of Fig. 1a). The network of pores provides short diffusion paths for electrolyte ions. As a result, the electrochemical performance of the composite is expected to be better than what can be achieved with planar current collectors. Fig. 1a reveals the Ni foam surface to be uniformly covered by the composite of PProDOT, carbon micro-spheres and Bi nanoflakes. Fig. 1b shows a magnified view, which clearly shows that the composite uniformly coats the Ni fibers and the apparent textured morphology is an indicator of multiple active sites available for electron transfer, when used as a CE in the photovoltaic part, and for ion and electron transfer/transport, when used as a redox active material in the supercapacitor part. Pristine PProDOT (Fig. 1c) is composed of agglomerated interconnected polymer particles, with cauli-flower like shapes, consistent with the structures usually obtained for CPs grown by electropolymerization.[34] Carbon micro-spheres are largely composed of spheres with irregularly shaped particles juxtaposed in-between the spheres. The spheres are approximately 5 to 15 μm in dimensions (Fig. 1d and e).

Bi nanoflakes, appear as large florets made up of discrete flakes (Fig. 1f), and the inter-flake gaps can potentially serve as active centers for electron transfer during the solar conversion, and as sites for accepting ions, during charge–discharge of the supercapacitor. The corresponding lattice scale image shows the flakes to be highly crystalline, having parallely oriented lattice fringes with an inter-fringe distance of 3.26 Å (Fig. 1g). This separation matches with an interplanar "*d*" spacing of 3.26 Å of the rhombohedral crystal lattice of Bi (PDF no: 85-1331). It is assigned to the (012) plane of Bi. An XRD pattern of Bi nanoflakes confirms the same, for it displays multiple peaks at 2θ of 22.6°, 27.2°, 38.1°, 39.7°, 44.7°, 46.1°, 48.8°, 56.2°, 62.5° and 64.7° with *d*-spacings of 3.93, 3.26, 2.35, 2.26, 2.02, 1.96, 1.86, 1.63, 1.48 and 1.43 Å, aligning with the (003), (012), (104), (110), (015), (006), (202), (024), (116) and (122) planes of the rhombohedral structure of Bi (Fig. 1h).[35] The XRD pattern of PProDOT shows three broad humps at 2θ of 24.4°, 44.2 and 62.5°. The most intense hump is close to the (002) plane of graphitic carbon (PDF: 74-2330) with $d = 3.6$ Å (Fig. 1i). It is ascribed to the intermolecular $\pi-\pi^*$ stacking of the polythiophene rings.[34] Carbon micro-spheres show peaks at 2θ of 26.1°, 43.4° and 54.1° with *d* values 3.4, 2.1, and 1.7 Å corresponding to the (002), (101) and (004) planes of hexagonal graphite (PDF: 75-1621) (Fig. 1j). Fig. 1k and l show the Raman spectra of PProDOT and carbon micro-spheres. PProDOT exhibits five prominent peaks at 1100, 1265, 1417, 1485 and 1548 cm^{-1}, attributed to the bending mode of the C–O–C group in the propylenedioxy ring, intermolecular $C_\alpha-C_{\alpha'}$ inter-ring stretching mode, symmetric $C_\alpha=C_\beta(-O)$ stretching vibration on the 5-membered ring, and symmetric and asymmetric intra-ring $C_\alpha=C_\beta$ vibrations.[34] Carbon micro-spheres produce two distinct peaks at 1360 (D-band) and 1599 (G-band) cm^{-1} corresponding to disordered carbon and in-plane bond stretching of the sp^2 hybridized carbon atoms as in graphitic carbon.[36]

3.2 Compositional aspects of SNGPs

S- and N-doped graphene particles (SNGPs) were incorporated in the TiO₂/SNGP/CdS photoanode to ameliorate the photovoltaic performance, by virtue of (1) their high electrical conductivity induced by the presence of the hetero (S and N) atoms *in lieu* of some of the carbons in the carbon backbone of the graphene particles, and (2) their ability to harvest visible light, which allows them to serve as co-sensitizers along with CdS in the TiO₂/SNGP/CdS photoanode. TEM images of (SNGP) (Fig. 2a) show them to have a wide distribution in size, ranging from 30 to 160 nm. A high resolution image (Fig. 2b) shows an inter-fringe distance of 0.35 nm (Fig. 2c), matching well with 0.34 nm, the interplanar spacing in hexagonal graphite. The Raman spectrum of SNGPs (Fig. 2d) shows two broad bands, and the curve fitting yields two peaks at 1334 and 1576 cm^{-1} corresponding to the D and the G bands. They are related to the sp^3 distortion in graphene and sp^2 hybridized graphitic carbon.[37]

Fig. 2e shows the full scan XPS spectrum of SNGPs in which the peaks at 532, 400.2, 284.5, 228 and 164.6 eV, are assigned to the O1s, N1s, C1s, S2s and S2p signatures respectively, revealing
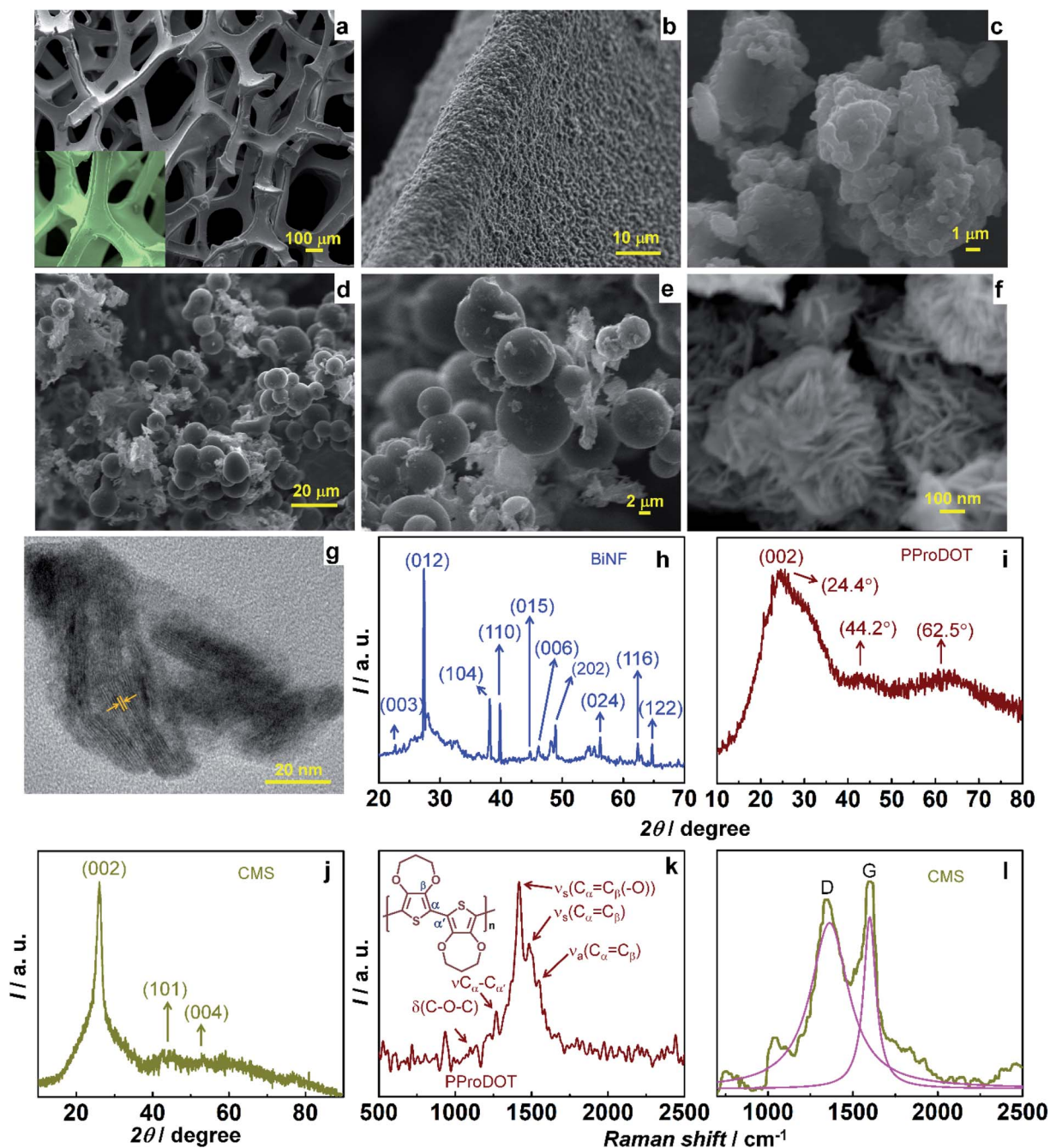
Fig. 1 SEM images of (a and b) PProDOT/CMS-BiNF@Ni foam (inset of (a) Ni foam), (c) PProDOT, (d and e) CMS and (f) BiNF. (g) TEM image of Bi nanoflakes. XRD patterns of (h) PProDOT, (i) CMS and (j) BiNF. Raman spectra of (k) PProDOT and (l) CMS. (CMS: carbon micro-spheres, BiNF: Bi nanoflakes).

the doping of S- and N- on graphene particles.[37] A deconvoluted C1s spectrum exhibits three components at 284.6 and 285.3 and 288.5 eV attributed to the C–C, (C–N/C–S/C–O) and C=O bonds respectively (Fig. 2f). The N1s spectrum is resolved into three peaks at 398.9, 400.5 and 401.7 eV which originate from the pyridinic, pyrrolic and graphitic – type nitrogen in the carbon framework (Fig. 2g). An S2p spectrum is resolved into three peaks at 163.7, 164.6 and 168.7 eV and while the former two represent the spin–orbit split components of S2p$_{3/2}$ and S2p$_{1/2}$

with a peak separation of 4 eV and an intensity ratio of 2 : 1, the latter peak stems from an oxidized sulfur group (Fig. 2h). Thus, the presence of nitrogen and sulfur in the graphene particles is confirmed. The electrical conduction capability of SNGPs is affirmed from linear sweep voltammetry, performed using a two probe system. On a clean glass substrate, SNGP solution was drop-cast and heated for 3 h at 80 °C. Two "SS all pins" were positioned vertically with their tips gently contacting the surface of the SNGP film without puncturing the same and then
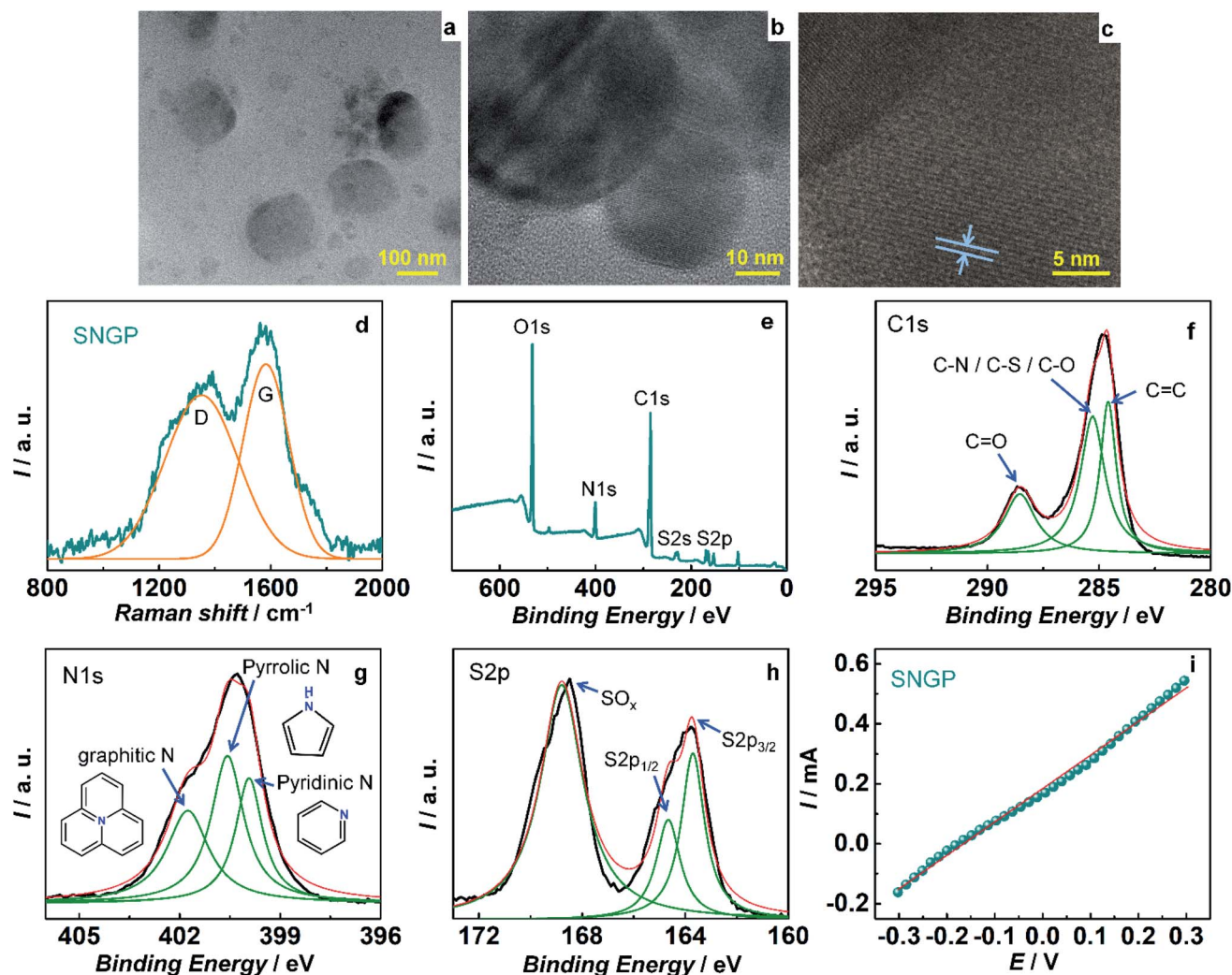
Fig. 2 (a and b) TEM images, (c) lattice scale image and (d) Raman spectrum of SNGPs. XPS spectra: (e) survey spectrum, and deconvoluted core level spectra for (f) C1s, (g) N1s and (h) S2p of SNGPs. (i) $I–V$ characteristics of SNGPs.

connected to a potentiostat. $I–V$ measurements were done over a voltage range of -0.3 to 0.3 V, and from the linear fit, the conductance of SNGPs is determined by employing the relation: $\Delta I/\Delta V = 1/R = $ slope (G) and it is 1.1 mS (Fig. 2i). This conductance is sufficient for channelizing the photo-excited electrons from CdS to TiO$_2$, thereby suppressing back electron transfer to the oxidized polysulfide species in the electrolyte at the TiO$_2$/SNGP/CdS/S$_n{}^{2-}$ interface in the solar cell part of the PSC, during the PSC operation.

3.3 Light harvesting and charge transfer in the TiO$_2$/SNGP/CdS photoanode

Fig. 3a and b reveal the optical absorption spectra of TiO$_2$, CdS and SNGPs and their composites. TiO$_2$, the underlying semiconducting support, exhibits a strong absorbance peak in the UV region; from the band edge that lies at 389.9 nm, E_g is estimated to be 3.18 eV. CdS, exhibits a broad absorption spanning the blue-green region of the visible spectrum, and the absorption edge is positioned at 546.2 nm which leads to an E_g

of 2.27 eV. SNGPs show two intense peaks with λ_{max} at 331 nm and 592 nm; they absorb strongly in the UV region and in the green-red region of the visible spectrum. These peaks are assigned to the n–π* transitions that originate from the C=O groups and the C–N linkages respectively.[38] From the absorption edge at 650 nm, the optical band gap (E_g) is determined to be 1.9 eV. The differences in the absorption profiles of CdS and SNGPs, clearly bring out their abilities to serve as co-sensitizers. In the photoanodes, the cumulative absorption features of the concerned components are perceivable. The TiO$_2$/CdS photoanode shows a peak in the UV region which extends to the visible region, over the 400 to 500 nm range, and the TiO$_2$/SNGP shows two peaks with λ_{max} at 328 nm and 613 nm. The ternary TiO$_2$/SNGP/CdS photoanode harvests solar radiation spanning from UV to almost all of the visible region, suggestive of how effective the complementary of two sensitizers can be in leading to a highly efficient solar cell.

To assess the excited state electron transfer and propagation in the TiO$_2$/SNGP/CdS photoanode, fluorescence spectra of

Paper

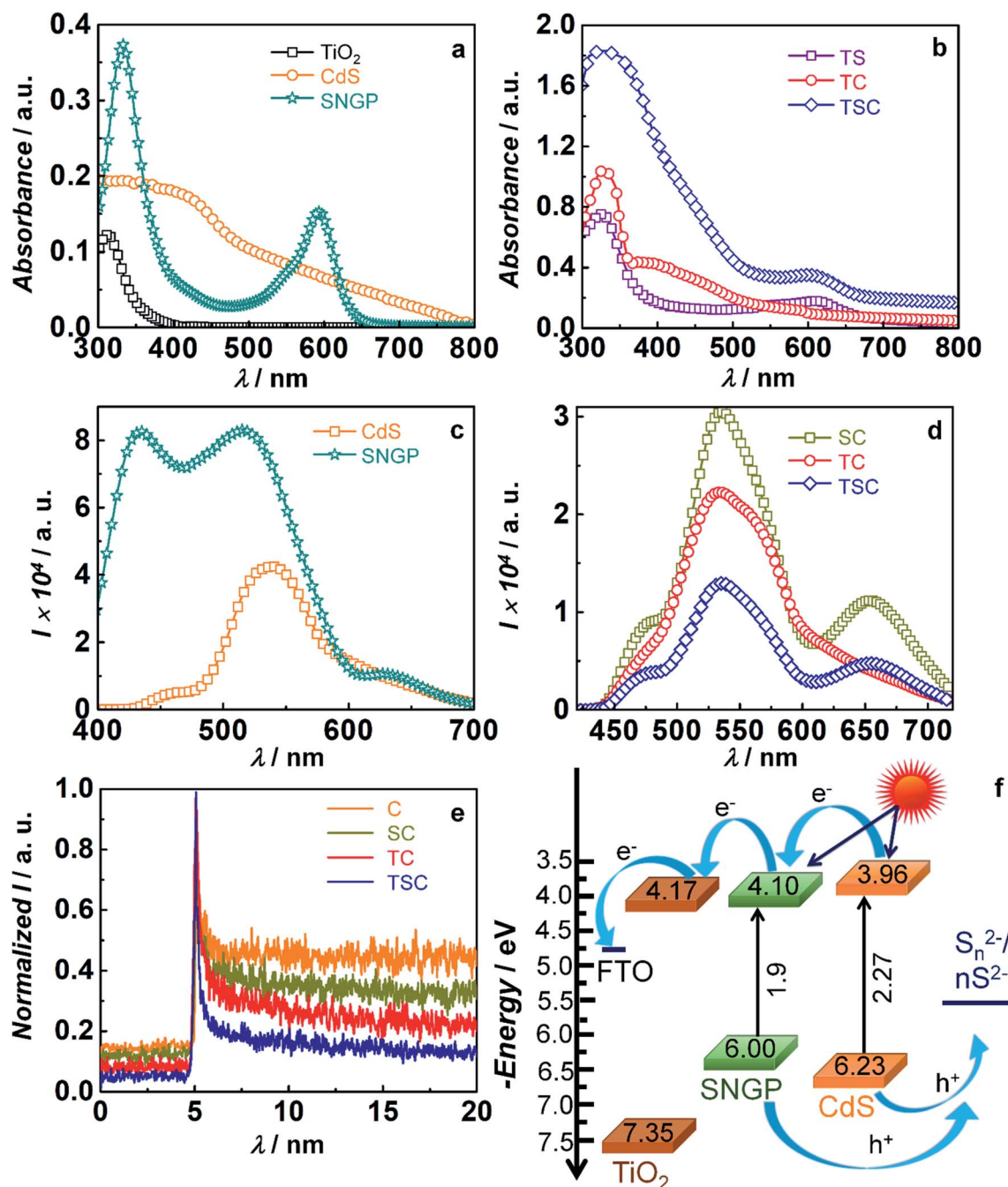Fig. 3 Absorbance spectra of (a) TiO$_2$, CdS and SNGPs and (b) TiO$_2$/SNGPs (TS), TiO$_2$/CdS (TC) and TiO$_2$/SNGP/CdS (TSC). Fluorescence spectra of (c) CdS (C), SNGPs and (d) SNGP/CdS (SC), TiO$_2$/CdS, and TiO$_2$/SNGP/CdS composites recorded at λ_{ex} of 370 nm. (e) Emission decay plots for photoactive electrodes measured at an λ_{ex} of 370 nm and at an λ_{em} of 534 nm. (f) Energy level diagram of the TiO$_2$/SNGP/CdS photoanode.

pristine CdS, SNGPs and their composite photoanodes, were recorded and are displayed in Fig. 3c and d. SNGPs, when excited at λ_{ex} of 370 nm, yields three emission peaks with λ_{max} positioned at 433, 515 and 633 nm. Possible transitions due to the different chromophores present in SNGPs, in the form of C=O, C–S, C–N covalent linkages, could be the reasons for the multiple bands. CdS produces a broad emission over the 500–600 nm span with a λ_{max} at 534 nm; it is assigned to the band edge recombination. Transitions between the intra-gap trap

states induces the broadness.[39] The SNGP/CdS composite has a fluorescence profile resembling that of CdS, but has a lowered overall intensity by about 28%. TiO$_2$/CdS and TiO$_2$/SNGP/CdS photoanodes show quenched emission bands, with intensities reduced by 47.7% and 69% relative to CdS. SNGPs produce a distinct band in the 600–700 nm range, which is not observed in TiO$_2$/CdS. This quenching is attributed to the transfer of photo-generated electrons from the conduction band (CB) of CdS to the CB of TiO$_2$ via SNGPs (if present) through the cascade

mechanism process. It is also observed that the SNGP's fluorescence peak with a λ_{max} at 433 nm is completely quenched in both SNGP/CdS and TiO$_2$/SNGP/CdS, indicating transfer of photo-generated electrons from SNGPs to FTO and TiO$_2$ respectively.

Fig. 3e shows the time-correlated single photon counting (TCSPC) measurements for the photoactive electrodes at excitation and emission wavelengths of 370 nm and 530 nm. Here, a bi-exponential function is used for fitting the parameters. The fitted parameters are given in Table S1 (ESI†). The average lifetimes for photoanodes are evaluated by using the equation given below,
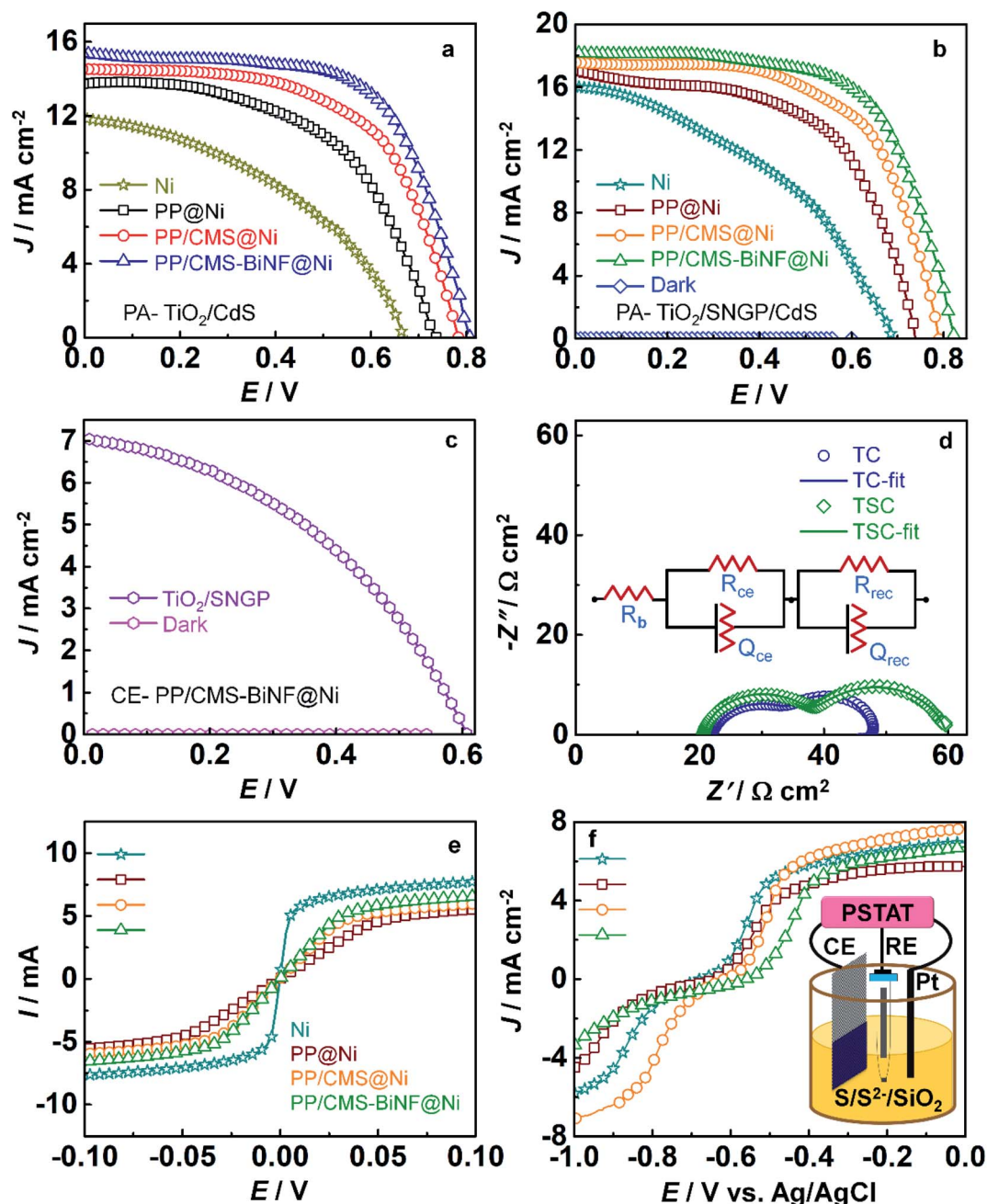
$$I = B_1 \exp(-t/\tau_1) + B_2 \exp(-t/\tau_2). \tag{1}$$

Fig. 4 J−V plots of solar cells with (a) TiO$_2$/CdS and (b) TiO$_2$/SNGP/CdS photoanodes with four different CEs: Ni foam, PProDOT@Ni foam, PProDOT/CMS@Ni foam and PProDOT/CMS-BiNF@Ni foam in a polysulfide/silica gel electrolyte under 1 sun illumination and in the dark. (c) J−V plots of a TiO$_2$/SNGP-S/S^{2-}/silica gel-PProDOT/CMS-BiNF@Ni foam cell under 1 sun illumination and in the dark. (d) EIS spectra of TiO$_2$/CdS (TC) and TiO$_2$/SNGP/CdS (TSC) photoanodes in a S/S^2/silica gel and PProDOT/CMS-BiNF@Ni foam in the dark. (e) I−V plots of Ni foam, PProDOT@Ni foam, PProDOT/CMS@Ni foam and PProDOT/CMS-BiNF@Ni foam. (f) Linear sweep voltammetry plots of different CEs: Ni foam, PProDOT@Ni foam, PProDOT/CMS@Ni foam and PProDOT/CMS-BiNF@Ni foam in a three-electrode system using S/S^{2-}/silica gel electrolyte. (PP: PProDOT, CMS: carbon micro-spheres, BiNF: Bi nanoflakes).

Thus, the electron lifetime is calculated using the equation,

$$\langle \tau \rangle = \Sigma B_i \tau_i^2 / \Sigma B_i \tau_i. \tag{2}$$

In eqn (1) and (2), I is the normalised emission intensity, τ_1 and τ_2 are the electron lifetime decay constants, B_1 and B_2 are the amplitude coefficients and τ is the average electron lifetime. The average lifetime for CdS of 17.2 ns, is reduced to 9 and 6.1 ns respectively for FTO/SNGP/CdS and TiO$_2$/CdS electrodes. Charge injection from the CB of CdS to the CB of SNGPs and subsequently to FTO in the former and from CdS to TiO$_2$ in the latter are energetically favorable processes, and occur spontaneously when impinged by a monochromatic radiation. Average lifetime for the ternary photoanode of TiO$_2$/SNGP/CdS, further drops to 1.7 ns, affirming efficient charge relay from CdS to SNGP to TiO$_2$. This reduced lifetime also implies that back electron transfer to the electrolyte will be minimized for this co-sensitized photoanode, compared to TiO$_2$/CdS, when used in a solar cell. An energy band diagram illustrating the positions of CBs and valence bands (VBs) of TiO$_2$, SNGPs and CdS and the direction of charge transfer can be seen in Fig. 3f. Cyclic voltammetry (CV) plots (Fig. S1, ESI†) were used to determine the CBs and by subtracting the optical E_g from the CB, the VBs were estimated. The values of CB, E_g and VB are summarized in Table S2 (ESI†). Upon excitation, in the TiO$_2$/SNGP/CdS photoanode, while hole transfer is thermodynamically feasible from the VB of CdS to the S^{2-} species in the electrolyte, the VB positions of CdS and SNGPs do not permit the same. However, since we obtained a superior PCE for TiO$_2$/SNGP/CdS (9.4%) compared to TiO$_2$/CdS (7.7%) and TiO$_2$/SNGP (1.7%) based solar cells, and a finite PCE of 0.6% for the FTO/SNGP/CdS cell as well (Fig. S2†); we conclude that the Fermi level or the intra-gap trap states which are positioned above the VB in CdS, allow for hole transfer, thus completing the circuit, and leading to the high efficiency.

3.4 SNGPs and the PProDOT/CMS-BiNF composite CE enhance PV performance

Before fabricating the PSC, the solar cell configuration is optimized by comparing the J–V characteristics of cells with two different photoanodes: TiO$_2$/CdS and TiO$_2$/SNGP/CdS, and with four different CEs (Fig. 4a and b). The CEs are: (1) bare Ni foam, coatings of (2) PProDOT, (3) the PProDOT/CMS composite and

(4) the PProDOT/CMS-BiNF composite deposited on Ni foam. Polysulfide/silica gel is served as the electrolyte or hole transport material. Each cell was exposed from the rear side to a 1 sun irradiance (100 mW cm^{-2}). Photovoltaic parameters are enumerated in Table 1 and the five cell averages are collated in Table S3 (ESI†). Among these cells, the TiO$_2$/CdS/gel/Ni foam cell delivers the lowest PCE of 3.3% with a short circuit current density (J_{SC}) of 11.82 mA cm^{-2}, an open circuit voltage (V_{OC}) of 676 mV and fill factor (FF) of 0.41. However, by wedging SNGPs in between the TiO$_2$ and CdS photoanode with the same CE, J_{SC} and V_{OC} increase to 16.08 mA cm^{-2} and 685 mV, and the PCE is enhanced to 4.5%. When light impinges, both CdS and SNGPs undergo electron–hole separation and photo-generated electrons cascade from the CB of CdS to that of SNGPs, and TiO$_2$ in that order. The additional CB of SNGPs between TiO$_2$ and CdS and its' electrical conduction properties accelerate the passage of electrons to TiO$_2$. The role of the CE in improving the PV response, is reflected in the PCEs when the composite PProDOT/CMS-BiNF replaces the bare Ni foam as the CE. PCEs escalate from 3.3 to 7.7% with TiO$_2$/CdS and from 4.5 to 9.4% with a TiO$_2$/SNGP/CdS photoanode. This PProDOT/CMS-BiNF composite CE imparts 2.3 and 2.1 times enhancements in the PCEs for the cells with the said photoanodes, in comparison with bare Ni foam CE.

The PCE difference from bare Ni foam to the PProDOT/CMS-BiNF composite reveals that the PProDOT/CMS-BiNF offers a low charge transfer resistance at the CE/electrolyte interface, allowing unhindered electron injection to the S$_n^{2-}$ species in the electrolyte and also furnishes a high electrocatalytic activity for the reduction of S$_n^{2-}$ species, thereby maximizing the overall charge separation, and resulting in the highest efficiencies, when combined with a given photoanode. PProDOT and CMS are electroactive materials, where PProDOT can conduct both ions and electrons via doping and de-doping, and CMS spheres can conduct electrons through the conjugated carbon framework. Bi nanoflakes improve the overall electroactivity of this electrode, by providing more number of active sites for electron accumulation. Together, the PProDOT/CMS-BiNF electrode is capable of transferring electrons rapidly to the electrolyte. The champion cell of the TiO$_2$/SNGP/CdS photoanode with the PProDOT/CMS-BiNF composite CE achieves the highest PCE of 9.4% with J_{SC} of 18.2 mA cm^{-2}, V_{OC} of 822 mV and an FF of 0.63 respectively. The synergy between (1) the co-sensitization effect

Table 1 Solar cell parameters of cells with different configurations under 1 sun illumination (100 mW cm^{-2}), cell exposed area: 0.1–0.11 cm^{-2}. The electrolyte is S/S^{2-}/silica gel

Solar cell configuration	J_{OC} (mA cm^{-2})	V_{OC} (V)	FF	η (%)	$\eta_{average}$ (%)
TiO$_2$/CdS–Ni	11.82	0.676	0.41	3.33	3.29 ± 0.03
TiO$_2$/CdS–PP@Ni	13.84	0.736	0.54	5.47	5.40 ± 0.06
TiO$_2$/CdS–PP/CMS@Ni	14.56	0.783	0.59	6.72	6.64 ± 0.05
TiO$_2$/CdS–PP/CMS-BiNF@Ni	15.40	0.807	0.63	7.83	7.74 ± 0.08
TiO$_2$/SNGP/CdS–Ni	16.08	0.685	0.41	4.53	4.50 ± 0.03
TiO$_2$/SNGP/CdS–PP@Ni	17.07	0.740	0.56	7.10	7.08 ± 0.04
TiO$_2$/SNGP/CdS–PP/CMS@Ni	17.61	0.790	0.60	8.42	8.34 ± 0.06
TiO$_2$/SNGP/CdS–PP/CMS-BiNF@Ni	18.2	0.822	0.63	9.50	9.41 ± 0.06
TiO$_2$/SNGP–PP/CMS-BiNF@Ni	7.05	0.606	0.41	1.77	1.72 ± 0.03

of SNGPs and CdS, which results in broader solar spectrum absorption and conversion at the TiO_2/SNGP/CdS photoanode and (2) the high electrocatalytic activity of the PProDOT/CMS-BiNF composite CE comes to the fore in the TiO_2/SNGP/CdS–S_n^{2-}/nS^{2-}–PProDOT/CMS-BiNF solar cell, and is responsible for the highest PCE delivered by this cell, in this work.

The role of SNGPs to serve as an independent photosensitizer was evaluated by recording the J–V response of a TiO_2/SNGP-S_n^{2-}/nS^{2-}–PProDOT/CMS-BiNF solar cell under 1 sun and in the dark (Fig. 4c). The cell delivers a PCE of 1.77% with a J_{SC} of 7 mA cm^{-2}, V_{OC} of 606 mV and an FF of 0.41 respectively, confirming the ability of SNGPs to function as a material capable of undergoing charge separation upon irradiance. In the dark, the same cell delivered a PCE of 0.07%, which is insignificant compared to the performance under illuminance. We have compared our data with solar cells based on graphene QDs, and also with solar cells based on conducting polymers (CPs) and metal nanoparticle/CP composites and we find that the PCE of 9.4% reported herein for the best cell with an average η of 9.4 ± 0.06%, is significantly enhanced compared to the reported PCEs, which are in the range of 0.6 to 8%.[40–44]

Metal sulfides are prone to irradiance induced photo-corrosion. The fumed silica in the S/S^{2-} gel electrolyte inhibits the photo-corrosion of CdS and leakage of the polysulfide electrolyte. It serves as a nano-filler for solidifying the electrolyte and enhancing the mechanical strength. The –OH on SiO_2 groups have a propensity to bind electrostatically to Cd^{2+}, and thus prevent hole injection to any dissolved oxygen in the electrolyte, which is one of the principal mechanisms for photo-corrosion, as shown in Fig. S3a (ESI†). Excess of photogenerated holes at the CdS surface, which are not consumed by the electron donors, i.e., the S^{2-} species in the electrolyte, are susceptible to reacting with oxygen, resulting in the formation of $CdSO_4$.[45] SiO_2 effectively reduces this photodissolution of CdS. SiO_2 also offers an energy barrier for the recombination between photo-generated electrons from the QDs and the oxidized S_n^{2-} species as well as for the recombination between the electrolyte and the injected electrons from TiO_2.[46] Furthermore, reduced graphene oxide (RGO) has also been shown to inhibit the photo-corrosion of CdS in a photocatalytic system.[47] Here too, the vicinal SNGPs provide suitably aligned energy states for the rapid extraction of the photo-excited electrons from CdS.

The stability tests for the cell with the following configuration: TiO_2/SNGP/CdS-polysulfide/silica gel-PProDOT/CMS-BiNF and the variation of photovoltaic parameters as a function of illumination time (to 1 sun or 100 mW cm^{-2}) are shown in Fig. S3b (ESI†). J–V characteristics of this cell were measured at every 2 h interval and the solar cell parameters are given in Table S4.† When the cell was measured for the first time, the PCE was 9.4% with J_{SC} of 18.16 mA cm^{-2}, V_{OC} of 0.81 V and an FF of 0.63 respectively. After 10 h, it still gave a PCE of 8.82%, which is lowered by ∼6.2% compared to the initial value. In the past, for a QDSC with a TiO_2/CdS/CdSe/polysulfide/PbS-carbon black configuration, the PCE decreased from 3 to 2.7% after 1000 h of illumination, which corresponds to a 10% loss in PCE.[48] In another study of a TiO_2/CdS/CdSe based cell with

a CuS CE, the initial PCE of 4.22% decreased to 4.0% after 2 h of continuous illumination.[49] A cell with a TiO_2/CdSeS–ZnS photoanode and a Pt CE showed an initial PCE of 4.23% and, after 8 h of irradiation, it decreased to 2.32%, thus amounting to a loss in PCE by ∼45%.[50] The cell fabricated in this study is also able to endure prolonged exposure without undergoing significant deterioration, indicating the role of fumed silica particles, and SNGPs in imparting an acceptable stability to the system.

Nyquist plots for the cells with TiO_2/CdS and TiO_2/SNGP/CdS photoanodes and having the same CE of the PProDOT/CMS-BiNF CE with the polysulfide/silica gel electrolyte (Fig. 4d), further demystify the role of SNGPs. The measurements were executed in the dark over a frequency range from 0.1 Hz to 1 MHz having an ac amplitude of 20 mV and at an open circuit voltage of 0.8 V. Two semicircles are obtained for both cells, and the data was fitted into an electrochemical circuit of $[R_b(R_{CE} \times Q_{CE})(R_{rec} \times Q_{rec})]$ and these parameters are given in Table S5 (ESI†). R_b is assigned to the bulk resistance of the gel, R_{CE} and Q_{CE} are the resistance and corresponding constant phase elements at the CE/electrolyte interface, and R_{rec} and Q_{rec} are the resistance and corresponding constant phase elements at the photoanode/electrolyte interface. R_b for TiO_2/CdS and TiO_2/SNGP/CdS are 20.7 and 22.2 Ω cm^2 respectively which are almost equal. The TiO_2/CdS cell shows a lower recombination resistance (R_{rec}) of 11.5 Ω cm^2 than the same cell co-sensitized with SNGPs (21.6 Ω cm^2). Thus, electron–hole recombination is reduced at the TiO_2/CdS photoanode/polysulfide electrolyte interface when SNGPs are sandwiched between TiO_2 and CdS and results in significant improvement in the PCE. It is also reflected in the Bode phase plot (phase angle versus frequency) (Fig. S4, ESI†). The electron recombination time (τ_n) is determined by using the formula, $\tau_n = 1/2\pi f_{max}$, where f_{max} is the peak frequency. Thus, τ_n for TiO_2/CdS and TiO_2/SNGP/CdS photoanodes are 1.1 ms and 1.6 ms respectively. It reveals the role of TiO_2/SNGP/CdS in reducing the recombination with oxidized species of the polysulfide electrolyte.

3.5 Characteristics of CEs

Conductances of the four CEs: Ni foam, PProDOT, PProDOT/CMS and PProDOT/CMS-BiNF (the latter three deposited over Ni foam), were determined from their I–V characteristics, and the plots are shown in Fig. 4e. Linear fits were obtained over the domains, outside of the saturation regimes. By using Ohm's law: $V = I \times R$, from the slopes, the conductances follow the order: Ni foam (1 S) > PProDOT/CMS-BiNF@Ni foam (0.17 S) > PProDOT/CMS@Ni foam (0.15 S) > PProDOT@Ni foam (0.1 S). Although the bare Ni foam shows the highest electrical conductance, it does not have good electrocatalytic activity, and because of this reason, the solar cell performances are the lowest with bare Ni foam. A good compromise between conductance and electrocatalytic activity is essential for a good solar cell response. To compare the electrocatalytic activities, linear sweep voltammetry (LSV) plots were recorded in a three electrode system, where the four CEs, Ag/AgCl/KCl and Pt rod are used as working, reference and auxiliary electrodes in a polysulfide electrolyte (Fig. 4f). The cathodic peak at −0.59 V

versus Ag/AgCl is the standard reduction potential for the reduction of sulfide.[51] The CEs show peak reduction potentials at −0.59, −0.57, −0.55 and −0.52 V for Ni foam, PProDOT@Ni foam, PProDOT/CMS@Ni foam and PProDOT/CMS-BiNF@Ni foam respectively. PProDOT/CMS-BiNF@Ni foam allows reduction of S_n^{2-} at a lower negative bias, and exhibits a larger cathodic peak current density compared to the remaining electrodes, thus ratifying its ability to work as a more efficient CE than the others in the solar cell.

The electrocatalytic activity of Bi nanoflakes in the CE was verified from an LSV plot and a Nyquist plot shown in Fig. S5 (ESI†). Ni foam and BiNF@Ni show reduction potentials peak at −0.59 and −0.56 V respectively, indicating that while the overpotential is 0 V with blank Ni, the reduction potential required for this reduction is slightly lowered with BiNF. Similarly, Nyquist plots were compared for the Ni//Ni and the Ni@BiNF//BiNF@Ni symmetric cells, again with the polysulfide electrolyte over a frequency range of 1 MHz to 0.1 Hz. Two skewed semicircles are observed for the two cells based on Ni and Ni@BiNF. Here, BiNF@Ni shows a lower charge transfer resistance (14.6 Ω cm²) compared to Ni alone (19.2 Ω cm²). Thus, BiNF exhibits superior electrocatalytic activity compared to Ni foam alone, evidencing its ability to contribute to efficient charge separation in the TiO₂/SNGP/CdS-polysulfide/silica gel-PProDOT/CMS-BiNF cell.

3.6 Supercapacitor performance

To assess the energy storage properties of the CEs, cyclic voltammetry, galvanostatic charge–discharge measurement, and EIS studies were performed for symmetric cells of PProDOT//PProDOT and CMS-BiNF/PProDOT//PProDOT/CMS-BiNF, each containing a 1 M LiClO₄/PC/PMMA gel electrolyte. CV plots recorded at different scan rates in the range of 10 to 300 mV s⁻¹ over a voltage window of 0 to 1 V (Fig. 5a and b) are characterized by quasi-rectangular or leaf like shapes. Voltammograms of the CMS-BiNF/PProDOT//PProDOT/CMS-BiNF cell enclose larger areas, indicative of a superior capacitance compared to the PProDOT//PProDOT cell. GCD plots of the same cells measured over current densities ranging from 0.05 mA cm⁻² to 1 mA cm⁻² over a voltage window of 0 to 1 V (Fig. 5c and d) show almost triangular shapes for both cells, but the CMS-BiNF/PProDOT//PProDOT/CMS-BiNF cell is characterized by longer discharge times. Oxidation (de-doping form) and reduction (neutral form) reactions occurring in PProDOT are given by the following reaction.

$$(PProDOT)^{x+}:(ClO_4)_x^- \text{ (neutral)} + y(ClO_4^-) \leftrightarrows \\ (PProDOT)^{(x+y)+}:(ClO)_{(x+y)}^- \text{ (oxidized)} + ye^-. \quad (3)$$

In case of carbon micro-spheres and Bi nanoflakes, they predominantly store and release charge by EDL formation and its collapse. The areal capacitance (ASC), energy density (E) and power density (P) for these electrodes in two electrode mode are determined using the following equation described below and these parameter values are provided in Table 2.

$$ASC \text{ (F cm}^{-2}) = (2 \times I \times \Delta t)/\Delta V. \quad (4)$$

$$E \text{ (W h cm}^{-2}) = 0.5 \times ASC \times \Delta V^2/3600. \quad (5)$$

$$P \text{ (W cm}^{-2}) = 3600 \times E/\Delta t. \quad (6)$$

In the above equations, I is current density in A cm⁻², Δt is discharge time in s and ΔV is voltage window in V respectively. On decreasing the current density from 1 to 0.05 mA cm⁻², the discharge time increases for both cells. The PProDOT/CMS-BiNF electrode exhibits an ASC and E of 180.8 mF cm⁻² and 25.1 μW h cm⁻² compared to the pure PProDOT electrode (ASC = 117.7 mF cm⁻² and E = 16.3 μW h cm⁻²), which confirms that the charge storage capacity of the composite is enhanced in contrast to that of the pristine polymer, due to the availability of more number of electrochemically accessible active sites and lower charge transfer resistance, bestowed by the Bi nanoflakes and carbon micro-spheres. Carbon micro-spheres and Bi nanoflakes also serve as buffering layers for the polymer, PProDOT and prevent the swelling and shrinkage of the polymer during repetitive charge–discharge cycles. The role of Bi nanoflakes as a supercapacitor material is confirmed from CV and GCD plots over a voltage range from 0 to 1 V, given in Fig. S6 (ESI†). From the CV plot, a quasi-rectangular shape is observed in the scan rate range from 10 to 100 mV cm⁻². The GCD plot shows an almost triangular shape and the ASC, E and P are determined to be 12 mF cm⁻², 1.7 μW h cm⁻² and 0.05 mW cm⁻², by applying a current density of 0.05 mA cm⁻².

There is no redox peak observed in the CV plots. Bi nanoflakes increase the electrical conductivity of the electrode, and improve the overall charge storage response by functioning as a material that can allow electrical double layer formation. However, the composite electrode of PProDOT/CMS-BiNF stores and liberates charge *via* pseudocapacitive and EDL capacitance mechanisms, because PProDOT is a redox polymer, and undergoes oxidation and reduction during the anodic and cathodic sweeps. These processes are kinetically fast, and therefore redox peaks are not observed at the said scan rates of 10–300 mV s⁻¹ (Fig. 5a). However, in a CV plot for PProDOT recorded at a low scan rate of 2 mV s⁻¹ (Fig. S7, ESI†), oxidation and reduction peaks are clearly observed at 0.45 V and 0.3 V respectively. The reversible doping and de-doping reactions are responsible for the observed peaks (eqn (3)). These peak positions agree well with that observed for a PProDOT derivative, in a tetrabutylammonium hexafluorophosphate electrolyte.[52]

On comparing performances with the literature studies on conducting polymer based supercapacitors, we found a study by Xiang *et al.* that reported a spherical composite having a yolk–shell structure of PProDOT and resin-based carbon spheres (PProDOT/YRFC) and the solid structure of the same (PProDOT/SRFC) having specific capacitances (SCs) of 327.5 and 180.9 F g⁻¹ at a current density of 1 A g⁻¹. PProDOT/YRFC showed a SC retention of 87.3% after 10 000 charge/discharge cycles, owing to its uniformly dispersible fluffy structure.[53] Kim *et al.*, reported ternary silver/manganese oxide/polyaniline (Ag/MnO₂/PANI) thin films which exhibited a SC of 800 F g⁻¹ and a cycling
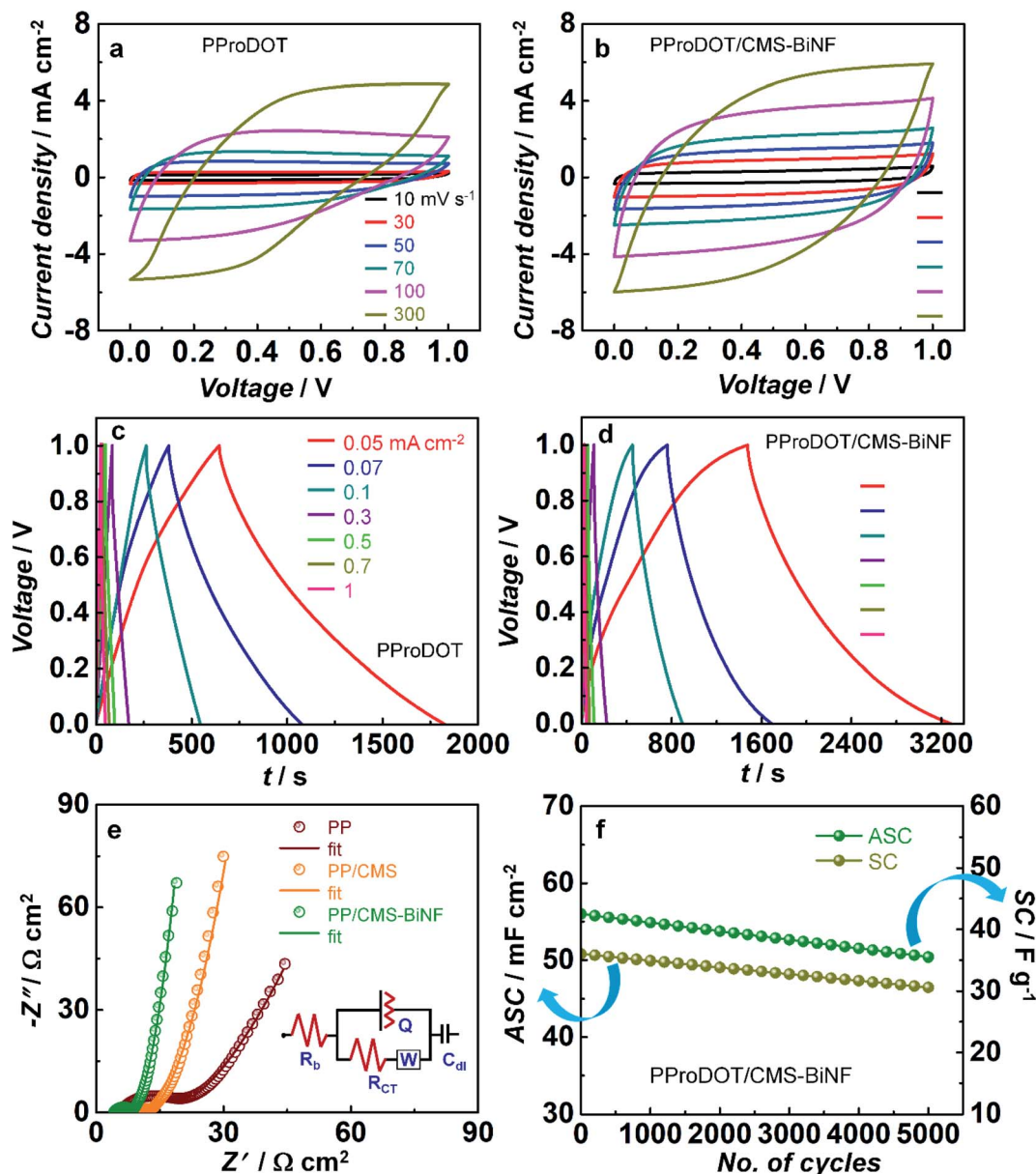
Fig. 5 CV plots (a) PProDOT and (b) PProDOT/CMS-BiNF coated Ni foam based symmetric cells recorded at different scan rates. Galvanostatic charge–discharge (GCD) curves of symmetric cells of (c) PProDOT and (d) PProDOT/CMS-BiNF at different current densities. (e) Nyquist plots of PProDOT, PProDOT/CMS and PProDOT/CMS-BiNF based symmetric cells at open circuit voltage from 0.1 Hz to 1 MHz and (f) ASC and SC *versus* number of cycles for the PProDOT/CMS-BiNF electrode and the equivalent circuit used for fitting the data. In (a–f), 1 M LiClO$_4$/PMMA gel served as the electrolyte. (PP: PProDOT, CMS: carbon micro-spheres, BiNF: Bi nanoflakes).

stability of up to 83% compared to the pure PANI polymer (66%).[54] A hierarchical N-doped porous carbon fiber@Cu (NPCF@Cu) composite based supercapacitor was reported by Hui *et al.*, where a SC of 210 F g^{-1} was achieved by NPCF@Cu-10 higher than NPCF@Cu-0 (130 F g^{-1}) and NPCF-10 (105 F g^{-1}) at a discharge current density of 50 F g^{-1}.[55] Cu NPs increased the electrical conductivity of the composite, allowed rapid electron transport and lowered the charge transfer resistance, thus maximizing the SC. A similar role is possibly played by Bi nanoflakes here, for the composite with Bi (PProDOT/CMS-BiNF) has a higher electrical conductance than that of PProDOT/CMS or PProDOT. Our values of SC are comparable to the literature reports.

EIS studies provide insights on charge transfer and transport phenomena in the supercapacitors. Fig. 5e shows Nyquist plots for symmetric cells of PProDOT, PProDOT/CMS and PProDOT/CMS-BiNF electrodes over a frequency range of 0.1 Hz to 1 MHz which show a distorted semicircle over the high to intermediate frequency range followed by an inclined straight line in the low frequency region. The data are fitted into a circuit of $[R_b(Q[R_{ct}W])C_{dl}]$. R_b, R_{ct}, Q, W and C_{dl} correspond to the bulk resistance of the electrolyte, charge transfer resistance at the

Table 2 Electrochemical properties of symmetric supercapacitors; active geometric area: 1 cm^2 and $\Delta V = 1$ V. All films are coated on Ni foam, and the electrolyte is LiClO$_4$/PMMA gel
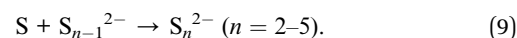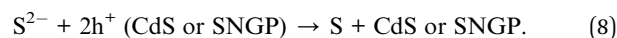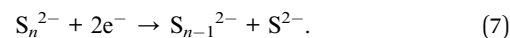
Current density, I (mA cm^{-2})	PProDOT//PProDOT			CMS-BiNF/PProDOT//PProDOT/CMS-BiNF		
	ASC (mF cm^{-2})	E (μW h cm^{-2})	P (mW cm^{-2})	ASC (mF cm^{-2})	E (μW h cm^{-2})	P (mW cm^{-2})
0.05	117.7	16.3	0.05	180.8	25.1	0.05
0.07	97.6	13.5	0.07	130.3	18.1	0.07
0.1	56.7	7.8	0.1	89.0	12.4	0.1
0.3	51.8	7.2	0.3	69.0	9.6	0.3
0.5	48.2	6.7	0.5	57.0	7.9	0.5
0.7	47.6	6.6	0.7	53.2	7.3	0.7
1	47.0	6.5	1	50.0	6.9	1

electrode/electrolyte interface, constant phase element, Warburg diffusion coefficient and double layer capacitance respectively. R_{ct} is the highest for the pure polymer cell, and comparable for the cells based on PProDOT/CMS and PProDOT/CMS-BiNF electrodes, indicating that carbon micro-spheres predominantly govern the interfacial resistance for charge transfer. The Warburg diffusion coefficient is the largest for PProDOT/CMS-BiNF (88.5 mΩ^{-1} cm^2) compared to PProDOT/CMS (49.5 mΩ^{-1} cm^2) and PProDOT (37 mΩ^{-1} cm^2) (Table S6, ESI†). This large difference in the magnitudes confirms that ion diffusion is more efficient across the cross-section of the PProDOT/CMS-BiNF electrode, suggestive of carbon micro-spheres and Bi nanoflakes playing active roles in facilitating ion transport. They tend to occupy the spaces in between the polymer chains or coils, and thus separate out the chains, permitting ions to easily move through. Fig. 5f shows ASC (mF cm^{-2}) and SC (F g^{-1}) *versus* number of cycles for the PProDOT/CMS-BiNF electrode measured at a current density of 1 mA cm^{-2} corresponding to a gravimetric current density of 0.66 A g^{-1} over a voltage window of 0 to 1 V. In the first cycle, the electrode produces an ASC of 56 mF cm^{-2}, while in the 5000th cycle it is characterized by an ASC of 47.6 mF cm^{-2}. Thus, there is 85% retention of its initial ASC. Similarly, SC reduces from 36 F g^{-1} to 30.6 F g^{-1} from the 1st to the 5000th cycle. Thus, 82% of the initial SC is preserved after cycling. The loss in SC or ASC, is possibly due to active material loss with cycling.
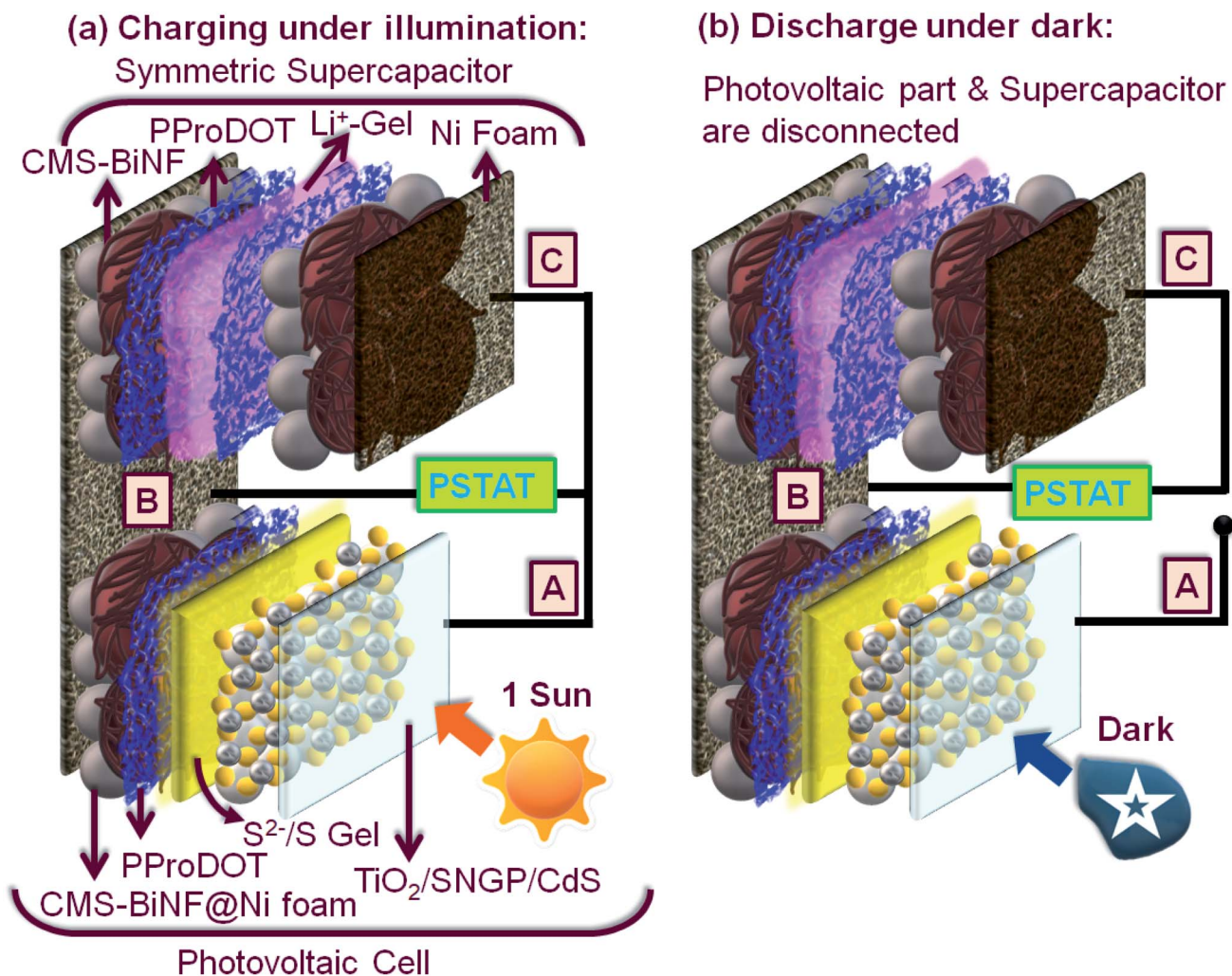
3.7 Working mechanism and performance of the PSC

The PSC comprises of two sandwich configurations supported on a single platform of a long Ni foam strip. (1) Solar cell: TiO$_2$/SNGP/CdS–S/S^{2-}/SiO$_2$ gel-PProDOT/CMS-BiNF@Ni foam and (2) symmetric supercapacitor: CMS-BiNF/PProDOT//PProDOT/CMS-BiNF encompassing a LiClO$_4$/PMMA gel. Scheme 3 furnishes a cartoon representation of the PSC. As per Scheme 3, for photo-charging the PSC, (A) and (C) are shorted, and this output and (B) are connected to the potentiostat in two electrode mode. When the PSC is illuminated under 1 sun (100 mW cm^{-2}) for 70 s, photo-excited electrons generated at the photoanode (A) reach (C) through the external circuit, *via* (C), they are relayed to the PProDOT/CMS-BiNF supercapacitor electrode. In this electrode in the as-fabricated state, PProDOT is present in the doped or oxidized state. During illumination, it accepts

electrons from the photoanode, and PProDOT undergoes de-doping or reduction to form the neutral polymer. Simultaneously, carbon micro-spheres and Bi nanoflakes also accept Li$^+$ ions from the electrolyte and store this charge *via* EDL formation. This reduction automatically drives oxidation at the opposite electrode, thereby releasing electrons which again travel through (B), and reach the CE of the solar cell part, where S$_n^{2-}$ species in the polysulfide electrolyte reduce to nS^{2-}. The sulfide ions diffuse through the polysulfide gel, scavenge the holes from the photosensitizers CdS and SNGPs, regenerating them, while simultaneously forming S$_n^{2-}$. The mechanism is given by the following reactions.

$$S_n^{2-} + 2e^- \rightarrow S_{n-1}^{2-} + S^{2-}. \tag{7}$$

$$S^{2-} + 2h^+ \text{ (CdS or SNGP)} \rightarrow S + \text{CdS or SNGP}. \tag{8}$$

$$S + S_{n-1}^{2-} \rightarrow S_n^{2-} \text{ } (n = 2\text{–}5). \tag{9}$$

These spontaneous reactions are evidenced from the photo-induced electrochemical parameters. Photovoltage *versus* time plots of PSCs based on symmetric supercapacitors based on the following electrodes: PProDOT, PProDOT/CMS and PProDOT/CMS-BiNF, are shown in Fig. 6a. In the first step, photo-charging was done, and no external voltage was applied. When illuminated by 1 sun (100 mW cm^{-2}), the PSCs based on the said symmetric supercapacitors are charged to voltages in the range of 0.7 to 0.8 V within a second, and this voltage is sustained for 70 s. At this juncture, the illumination is switched off, the solar cell (A) is disconnected, and the PSCs are discharged under galvanostatic conditions. Under an applied fixed current density of 0.033 mA cm^{-2}, the voltage across the PSC decays to zero volts for all the three supercapacitors. The discharge time is the longest for the ternary composite (PProDOT/CMS-BiNF) compared to PProDOT and PProDOT/CMS. Thus, the ASCs are calculated to be 104.6, 84 and 50.5 mF cm^{-2} for PProDOT/CMS-BiNF, PProDOT/CMS and PProDOT based PSCs respectively. The ASC, energy density (E) and power density (P) magnitudes are provided in Table 3. The higher ASC achieved by the PProDOT/CMS-BiNF electrode is attributed to the synergic interaction between the conducting polymer, carbon and metal nanoparticles, *i.e.*, pseudocapacitive behavior of PProDOT, large

(a) Charging under illumination:
Symmetric Supercapacitor

(b) Discharge under dark:
Photovoltaic part & Supercapacitor are disconnected

Scheme 3 Schematics of the PSC showing (a) charging under illumination and (b) discharging in the dark.

effective surface area and electrical conductivity of carbon and Bi nanoflakes. Thus the internal resistance is reduced and ion and electron transport are facilitated. Bi nanoflakes also prevent the aggregation of the carbon microspheres and PProDOT chains, thus preventing charge trapping. Furthermore, repeated shrinking and swelling of the polymer *via* redox reactions also deteriorate cell performance; this is alleviated by the interspersed carbon-microspheres and Bi nanoflakes, which accommodate the localized volume change experienced by the polymer, thus imparting better cycling stability to the composite.

To examine the rate capability of the PSCs, the photovoltage decay plots were recorded for the PProDOT/CMS-BiNF electrode based PSC at different discharge current densities, and they are shown in Fig. 6b. When the discharge current density increases from 0.033 to 0.67 mA cm^{-2}, the ASC varies from 104.6 to 27.1 mF cm^{-2}. The highest energy density of 8.9 μW h cm^{-2} is obtained at the discharge current density of 0.033 mA cm^{-2} (Table 4). The PSC shows a good performance at low current densities. Self-discharge *versus* time plot for 70 s under 1 sun illumination is compared in Fig. 6c for the PSCs based on symmetric

supercapacitors containing the PProDOT, PProDOT/CMS and PProDOT/CMS-BiNF electrodes. Both photo-charging and discharging (in the dark) of the PSC is performed without applying any voltage and discharge current. When the PSC is photo-charged for 70 s, a maximum voltage of 0.78 V is attained by the PProDOT/CMS-BiNF based cell. Once the light is switched off and solar cell is disconnected, there is an *IR* drop, the voltage drops to 0.7 V and gradually to 0.4 V at 500 s, and thereafter it remains constant. PSCs based on PProDOT/CMS and pure PProDOT show photovoltages of 0.74 V and 0.55 V, which decrease to 0.3 V and 0.17 V at 500 s. The *IR* drop is the least in case of the PProDOT/CMS-BiNF film, thus illustrating that this cell is superior to the other two cells.

Photocurrent *versus* time curves for the PSCs are shown in Fig. 6d. During photo-charging for 70 s, a photocurrent maximum of 8 mA cm^{-2} is generated for the PProDOT/CMS-BiNF electrode. It is produced by the photo-excited electrons in the TiO$_2$/SNGP/CdS photoanode of the solar cell, which are transmitted through the external circuit to the supercapacitor for charging, *i.e.*, from (A) to (C) in the PSC (Scheme 3a).[5] Thus, this current slowly decays to ~6 mA cm^{-2} after 70 s and it
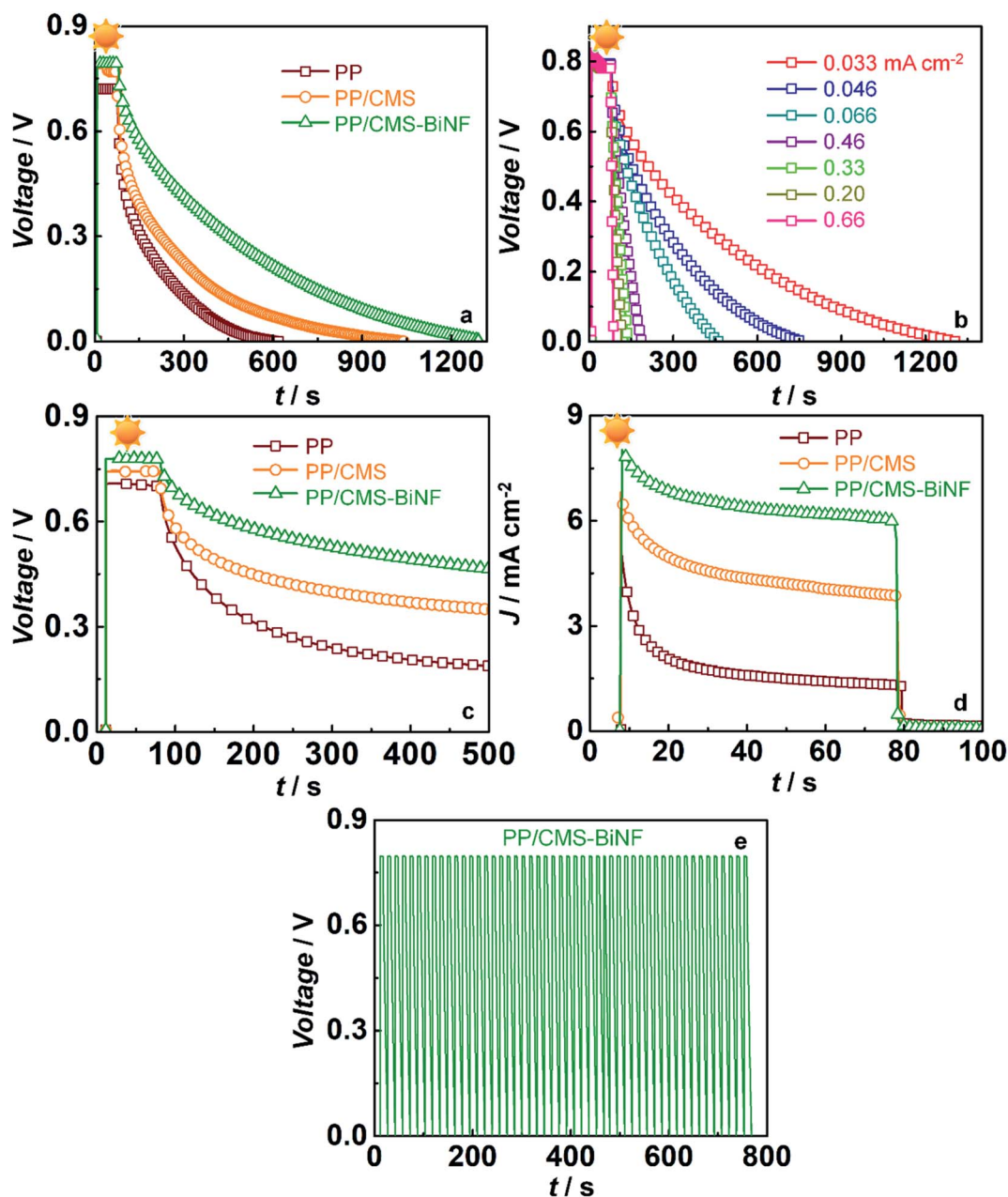
Fig. 6 (a) Voltage acquired by the PSCs under irradiance *versus* time for PProDOT, PProDOT/CMS and PProDOT/CMS-BiNF as CE and supercapacitor electrodes, and their subsequent discharge under applied current in the dark. (b) Voltage acquired by the PSC based on PPro-DOT/CMS-BiNF under irradiance *versus* time, followed by its discharge at different current densities in the dark or rate capability. (c) Self-discharge plots in the dark for PSCs with PProDOT, PProDOT/CMS and PProDOT/CMS-BiNF. (d) Photocurrent density *versus* time without applying bias for PSCs with PProDOT, PProDOT/CMS and PProDOT/CMS-BiNF as supercapacitor electrodes, (photo-charging is done under 1 sun illumination (100 mW cm^{-2}) and discharging is done in the dark). (e) Photo-charging and galvanostatic discharging *versus* time plot for the PProDOT/CMS-BiNF based PSC. (PP: PProDOT, CMS: carbon micro-spheres, BiNF: Bi nanoflakes).

Table 3 Storage parameters of the PSCs with the solar cell: a TiO$_2$/SNGP/CdS–S/S^{2-}/silica gel-PProDOT/CMS-BiNF CE and three different supercapacitor configurations, area of the supercapacitor electrode: 1.5 cm^2

Supercapacitor	Discharge current density (mA cm^{-2})	Voltage (V)	ASC (mF cm^{-2})	E (µW h cm^{-2})	P (mW cm^{-2})
PProDOT	0.033	0.72	50.5	3.6	0.024
PProDOT/CMS	0.033	0.77	84.0	6.9	0.025
PProDOT/CMS-BiNF	0.033	0.79	104.6	9.0	0.026

Table 4 Storage parameters of the PSCs with $TiO_2/SNGP/CdS-S/S^{2-}/$ silica gel-PProDOT/CMS-BiNF as the solar cell part and CMS-BiNF/PProDOT//PProDOT/CMS-BiNF as the supercapacitor part; area of supercapacitor electrode: 1.5 cm^2 and $\Delta V = 0.79$ V

Current density, I (mA cm^{-2})	ASC (mF cm^{-2})	E (μW h cm^{-2})	P (mW cm^{-2})
0.033	104.6	8.9	0.026
0.047	80.9	7.0	0.031
0.067	65.0	5.6	0.052
0.2	54.7	4.7	0.156
0.33	50.1	4.3	0.260
0.47	23.8	2.0	0.310
0.67	27.1	2.3	0.526

roughly remains the same for the remaining duration of illumination. When light is switched off, under dark conditions and still under short-circuit conditions, (A) and (C) remain electrically connected, the photocurrent abruptly drops to negligible (close to zero) values, inferring that the current passing through the circuit is purely generated by photo-excitation. Similar profiles for current were also observed with the PProDOT/CMS and PProDOT electrodes, although the overall magnitudes of photocurrent maxima and saturation currents were lower than that achieved with the PProDOT/CMS-BiNF electrode. With these electrodes too, the photocurrent drops sharply to insignificantly small values, in the light switch off mode. These studies confirm that the $TiO_2/SNGP/CdS-S/S^{2-}/$ SiO_2 gel-PProDOT/CMS-BiNF@Ni foam connected to the CMS-BiNF/PProDOT//PProDOT/CMS-BiNF cell on a common current collector platform has tremendous potential as a dual function single device.

The overall photo-conversion and storage efficiency ($\eta_{overall}$) of the PSC device is given by the following equation.

$$\eta_{overall} = (E_{PSC} \times A_{PSC})/(E_{light} \times t_{ch} \times A_{QDSC}). \quad (10)$$

In eqn (10), E_{PSC}, E_{light}, t_{ch}, A_{PSC}, and A_{QDSC} are the energy density of PSC, incident light power density (100 mW cm^{-2}), photo-charging time, and the effective active surface areas of the supercapacitor part and the solar cell part of the PSC respectively. The energy storage efficiency of the PSC is given by the following equation.

$$\eta_{storage} = \eta_{overall}/\eta_{conversion} \quad (11)$$

In eqn (11), $\eta_{storage}$ is the energy storage efficiency of the supercapacitor part in the PSC and $\eta_{conversion}$ is the PCE of the solar cell in the PSC (9.41%). Thus, $\eta_{overall}$ and $\eta_{storage}$ of the PSC device are determined to be 6.8% and 72.3% respectively. Previously, Xu et al.,[56] proposed a PEDOT-carbon supercapacitor integrated with the perovskite solar cell. The PSC reveals an $\eta_{overall}$ of 4.7% and an $\eta_{storage}$ of 73.77% respectively. Zhang et al.,[57] reported an energy fiber PSC based on an integrating polymer solar cell with MWCNT sheets wrapped on a titania nanotube-modified Ti wire based supercapacitor. An $\eta_{overall}$ of 0.79% is obtained for this energy fiber device. A summary of $\eta_{conversion}$, $\eta_{overall}$ and $\eta_{storage}$ of PSCs is listed in Table S7 (ESI†).

The cycling stability of the PSC can be gauged from Fig. 6e. The ASC versus time graph is plotted under light on/off conditions for 50 cycles. Photo-charging occurred for 5 s and galvanostatic discharging occurred after applying a discharge current density of 1 mA cm^{-2}. The PSC gives a stable voltage over 50 cycles, indicating its stability and capability for storing charges repetitively.

4. Conclusions

A dual function PSC that sequentially converts solar radiation into current and stores the same as charge was prepared with a novel photoanode and a new CE or charge storage electrode configuration. TiO_2 co-sensitized with SNGPs and CdS, where the doping of graphene particles by hetero-atoms of sulfur and nitrogen imparts a high electrical conductance of 1.1 mS, pronounced fluorescence over the entire visible region, effective charge separation ensured by its favorable conduction band position that minimizes recombination with the electrolyte, and the capability to harvest red photons efficiently when combined with the harvesting of the blue-green region by CdS, results in a remarkably high average PCE of 9.41 ± 0.06% for the solar cell, which is significantly greater than the PCEs reported for conventional Ru dye- or perovskite-based PSCs. While perovskites have issues of air-stability and toxicity, and Ru dyes are expensive, this ternary composite offers the following benefits: air-stability, relatively less toxicity (for CdS is stable, and can be disposed carefully), cheap components, low fabrication cost, and ease of scale-up, thus opening up avenues for its practical deployment. The unique electrode of the PProDOT/CMS-BiNF wherein the carbon micro-spheres and Bi nanoflakes are enmeshed with the PProDOT chains shows higher electrical conductance, better charge storage parameters: SC (180.8 mF cm^{-2}), E and P of 25.1 μW h cm^{-2} and 0.05 mW cm^{-2}, lower diffusional impedance and a greatly enhanced electrocatalytic activity for polysulfide reduction compared to that shown by the pristine polymer, PProDOT or PProDOT/CMS electrodes. These factors together result in an overall photo-conversion and storage efficiency of 6.8%, for the PSC with the following architecture: $TiO_2/SNGP/CdS$-gel-PProDOT/CMS-BiNF@Ni foam/CMS-BiNF/PProDOT//PProDOT/CMS-BiNF which is superior to that reported in the literature for different PSCs having conducting polymers like PEDOT or nanostructured carbons as the storage electrodes. The performance metrics of this PSC render it to be a yardstick device for use as a photo-powered energy system in practical applications.

Conflicts of interest

There is no conflicts of interest to declare.

Acknowledgements

thankful to Piu Chawdhury for recording TEM images of SNGPs and Bi nanoflakes.

References

1 C. H. Ng, H. N. Lim, S. Hayase, I. Harrison, A. Pandikumar and N. M. Huang, *J. Power Sources*, 2015, **296**, 169–185.

2 T. N. Murakami, N. Kawashima and T. Miyasaka, *Chem. Commun.*, 2005, 3346.

3 H. Nagai and H. Segawa, *Chem. Commun.*, 2004, 974–975.

4 C.-Y. Hsu, H.-W. Chen, K.-M. Lee, C.-W. Hu and K.-C. Ho, *J. Power Sources*, 2010, **195**, 6232–6238.

5 S. C. Lau, H. N. Lim, T. B. S. A. Ravoof, M. H. Yaacob, D. M. Grant, R. C. I. MacKenzie, I. Harrison and N. M. Huang, *Electrochim. Acta*, 2017, **238**, 178–184.

6 Z. Yang, L. Li, Y. Luo, R. He, L. Qiu, H. Lin and H. Peng, *J. Mater. Chem. A*, 2013, **1**, 954–958.

7 R. Liu, C. Liu and S. Fan, *J. Mater. Chem. A*, 2017, **5**, 23078–23084.

8 K. Gao, D. Ti and Z. Zhang, *Sustainable Energy Fuels*, 2019, **3**, 1937–1942.

9 X. Xu, S. Li, H. Zhang, Y. Shen, S. M. Zakeeruddin, M. Graetzel, Y.-B. Cheng and M. Wang, *ACS Nano*, 2015, **9**, 1782–1787.

10 J. Liang, G. Zhu, C. Wang, Y. Wang, H. Zhu, Y. Hu, H. Lv, R. Chen, L. Ma, T. Chen and Z. Jin, *Adv. Energy Mater.*, 2017, 7, 1601208.

11 J. Liang, G. Zhu, Z. Lu, P. Zhao, C. Wang, Y. Ma, Z. Xu, Y. Wang, Y. Hu, L. Ma and T. Chen, *J. Mater. Chem. A*, 2018, **6**, 2047–2052.

12 J. Liang, G. Zhu, C. Wang, P. Zhao, Y. Wang, Y. Hu, L. Ma, Z. Tie, J. Liu and Z. Jin, *Nano Energy*, 2018, **52**, 239–245.

13 S. Bose, T. Kuila, A. K. Mishra, R. Rajasekar, N. H. Kim and J. H. Lee, *J. Mater. Chem.*, 2012, **22**, 767–784.

14 P. V. Kamat, *J. Phys. Chem. Lett.*, 2011, **2**, 242–251.

15 D. Qu, M. Zheng, P. Du, Y. Zhou, L. Zhang, D. Li, H. Tan, Z. Zhao, Z. Xie and Z. Sun, *Nanoscale*, 2013, **5**, 12272.

16 W. K. Chee, H. N. Lim, Z. Zainal, N. M. Huang, I. Harrison and Y. Andou, *J. Phys. Chem. C*, 2016, **120**, 4153–4172.

17 Y. Li, Y. Zhao, H. Cheng, Y. Hu, G. Shi, L. Dai and L. Qu, *J. Am. Chem. Soc.*, 2012, **134**, 15–18.

18 B.-X. Zhang, H. Gao and X.-L. Li, *New J. Chem.*, 2014, **38**, 4615–4621.

19 T. Majumder, S. Dhar, K. Debnath and S. P. Mondal, *Mater. Res. Bull.*, 2017, **93**, 214–222.

20 M. Dutta, S. Sarkar, T. Ghosh and D. Basak, *J. Phys. Chem. C*, 2012, **116**, 20127–20131.

21 M.-H. Yeh, C.-P. Lee, C.-Y. Chou, L.-Y. Lin, H.-Y. Wei, C.-W. Chu, R. Vittal and K.-C. Ho, *Electrochim. Acta*, 2011, **57**, 277–284.

22 K. Saranya, M. Rameez and A. Subramania, *Eur. Polym. J.*, 2015, **66**, 207–227.

23 J. Yang, Y. Liu, S. Liu, L. Li, C. Zhang and T. Liu, *Mater. Chem. Front.*, 2017, **1**, 251–268.

24 B. Pandit, V. S. Devika and B. R. Sankapal, *J. Alloys Compd.*, 2017, **726**, 1295–1303.

25 K.-M. Lee, P.-Y. Chen, C.-Y. Hsu, J.-H. Huang, W.-H. Ho, H.-C. Chen and K.-C. Ho, *J. Power Sources*, 2009, **188**, 313–318.

26 S. Ahmad, J.-H. Yum, H.-J. Butt, M. K. Nazeeruddin and M. Grätzel, *ChemPhysChem*, 2010, **11**, 2814–2819.

27 J. Zhang, X. Li, W. Guo, T. Hreid, J. Hou, H. Su and Z. Yuan, *Electrochim. Acta*, 2011, **56**, 3147–3152.

28 S. Rafique, R. Sharif, I. Rashid and S. Ghani, *AIP Adv.*, 2016, **6**, 085018.

29 A. Kumar, D. M. Welsh, M. C. Morvant, F. Piroux, K. A. Abboud and J. R. Reynolds, *Chem. Mater.*, 1998, **10**, 896–902.

30 E. Frackowiak, V. Khomenko, K. Jurewicz, K. Lota and F. Béguin, *J. Power Sources*, 2006, **153**, 413–418.

31 N. H. Nabilah Azman, H. N. Lim and Y. Sulaiman, *Electrochim. Acta*, 2016, **188**, 785–792.

32 M. R. Rosario-Canales, P. Deria, M. J. Therien and J. J. Santiago-Avilés, *ACS Appl. Mater. Interfaces*, 2012, **4**, 102–109.

33 L. Ma, X. Shen, Z. Ji, G. Zhu and H. Zhou, *Chem. Eng. J.*, 2014, **252**, 95–103.

34 R. Jamal, L. Zhang, M. Wang, Q. Zhao and T. Abdiryim, *Prog. Nat. Sci.: Mater. Int.*, 2016, **26**, 32–40.

35 P. Subramanyam, T. Khan, G. Neeraja Sinha, D. Suryakala and C. Subrahmanyam, *Int. J. Hydrogen Energy*, 2020, **45**, 7779–7787.

36 X. Chen, K. Kierzek, Z. Jiang, H. Chen, T. Tang, M. Wojtoniszak, R. J. Kalenczuk, P. K. Chu and E. Borowiak-Palen, *J. Phys. Chem. C*, 2011, **115**, 17717–17724.

37 A. G. Kannan, J. Zhao, S. G. Jo, Y. S. Kang and D.-W. Kim, *J. Mater. Chem. A*, 2014, **2**, 12232–12239.

38 F. Lu, Y. Zhou, L. Wu, J. Qian, S. Cao, Y. Deng and Y. Chen, *Int. J. Opt.*, 2019, **2019**, 1–9.

39 P. A. Sant and P. V. Kamat, *Phys. Chem. Chem. Phys.*, 2002, **4**, 198–203.

40 V. M. Prabhagar, M. P. Kumar, C. Takahashi, S. Kundu, T. N. Narayanan and D. K. Pattanayak, *New J. Chem.*, 2019, **43**, 14313–14319.

41 M. Rahman, F. Xie, Y. Li and M. Wei, *J. Electroanal. Chem.*, 2019, **840**, 160–164.

42 A. Das, A. Kolay, S. M. Shivaprasad and M. Deepa, *Chem. Eng. J.*, 2019, **374**, 292–303.

43 C.-Y. Hsu, K.-M. Lee, J.-H. Huang, K. R. Justin Thomas, J. T. Lin and K.-C. Ho, *J. Power Sources*, 2008, **185**, 1505–1508.

44 S. Koussi-Daoud, D. Schaming, P. Martin and J.-C. Lacroix, *Electrochim. Acta*, 2014, **125**, 601–605.

45 B. Weng, M. Y. Qi, C. Han, Z. R. Tang and Y. J. Xu, *ACS Catal.*, 2019, **9**, 4642–4687.

46 H. Wei, G. Wang, J. Shi, H. Wu, Y. Luo, D. Li and Q. Meng, *J. Mater. Chem. A*, 2016, **4**, 4194–14203.

47 Y. Tang, X. Hu and C. Liu, *Phys. Chem. Chem. Phys.*, 2014, **16**, 25321–25329.

48 Y. Yang, L. Zhu, H. Sun, X. Huang, Y. Luo, D. Li and Q. Meng, *ACS Appl. Mater. Interfaces*, 2012, **4**, 6162–6168.

49 F. Wang, H. Dong, J. Pan, J. Li, Q. Li and D. Xu, *J. Phys. Chem. C*, 2014, **118**, 19589–19598.

50 K. Yan, W. Chen and S. Yang, *J. Phys. Chem. C*, 2013, **117**, 92–99.

51 Y. Cao, Y. Xiao, J.-Y. Jung, H.-D. Um, S.-W. Jee, H. M. Choi, J. H. Bang and J.-H. Lee, *ACS Appl. Mater. Interfaces*, 2013, **5**, 479–484.

52 M. G. Ersozoglu, H. D. Gilsing, A. Gencturk and A. S. Sarac, *Int. J. Electrochem. Sci.*, 2019, **14**, 9504–9519.

53 L. Xiang, A. Ali, R. Jamal, S. Ding, Z. Zhong and T. Abdiryim, *Polym. Compos.*, 2019, **40**, 1989–1999.

54 J. Kim, H. Ju, A. I. Inamdar, Y. Jo, J. Han, H. Kim and H. Im, *Energy*, 2014, **70**, 473–477.

55 Y. Hui, Y. Shewen, W. Yunfeng, Z. Jiaming, J. Jingwen, C. Jiahao, Z. Qinqin and L. Tongxiang, *J. Alloys Compd.*, 2019, **792**, 976–982.

56 J. Xu, Z. Ku, Y. Zhang, D. Chao and H. J. Fan, *Adv. Mater. Technol.*, 2016, **1**, 1600074.

57 Z. Zhang, X. Chen, P. Chen, G. Guan, L. Qiu, H. Lin, Z. Yang, W. Bai, Y. Luo and H. Peng, *Adv. Mater.*, 2014, **26**, 466–470.